Bioturbation and the $\delta^{56}Fe$ Signature of Dissolved Iron Fluxes from Marine Sediments

Sebastiaan J. van de Velde[1,2], Andrew. W. Dale[3], and Sandra Arndt[1]

[1] Department of Geoscience, Environment & Society, Université Libre de Bruxelles, Brussels, Belgium
[2] Operational Directorate Natural Environment, Royal Belgian Institute of Natural Sciences, Brussels, Belgium
[3] GEOMAR Helmholtz Centre for Ocean Research Kiel, Kiel, Germany

Corresponding author: Sebastiaan J. van de Velde (sebastiaan.van.de.velde@ulb.be)

Key Points:

- A diagenetic model capable of tracking iron isotope signatures was developed
- Bioturbation increases the global DFe release from marine sediments from 70 to 158 Gmol yr^{-1} and decreases its isotopic signature
- Decreasing ocean oxygen content by 40 µM increases global DFe release from marine sediments from 158 to 261 Gmol DFe yr^{-1}.

Abstract

Iron is a key limiting nutrient for phytoplankton. Continental shelf and slope sediments are important sources of dissolved iron (DFe). Stable iron isotopes ($\delta^{56}Fe$) are a particularly useful tool to quantify the DFe sources and sinks in the ocean. The isotopic signature of the sedimentary DFe source is controlled by environmental factors such as bottom water redox conditions, carbon oxidation and bioturbation by burrowing fauna, but the exact relation on a global scale is poorly understood. We developed a reaction-transport model capable of tracing dissolved iron isotope fractionation in marine sediments to quantify the isotopic signature of benthic DFe fluxes under a wide range of environmental conditions. We derived fractionation factors for iron reduction (-1.3‰), iron oxidation (+0.4‰), iron sulphide precipitation (+0.5‰) and dissolution (-0.5‰) and pyrite precipitation (-0.7‰) that were in line with existing literature. At bottom-water oxygen concentrations > 50 µM, bioturbation increased the benthic DFe flux and increased the $\delta^{56}Fe$ signature. In contrast, at bottom-water oxygen concentrations < 50 µM, bioturbation led to a decrease in the benthic DFe flux and its $\delta^{56}Fe$ value. On a global scale, a model simulation without bioturbation decreased the sedimentary DFe release from ~158 Gmol DFe yr^{-1} to ~70 Gmol DFe yr^{-1}, and decreased the variability in the $\delta^{56}Fe$ signature of the DFe flux. Finally, we find that a decrease in ocean oxygen content by 40 µM can increase global sedimentary DFe release by up to 103 Gmol DFe yr^{-1}.

Plain language summary

Iron is an important and limiting nutrient for marine phytoplankton, but the sources of iron to the ocean are not well quantified yet. A useful tool to constrain different sources of iron is using the stable iron isotopic signature, i.e. the ratio of heavy iron versus light iron. Iron recycled from the seafloor is an important source of iron, but its stable isotopic signature, as well as its relation to environmental conditions (bottom-water oxygen concentration, sediment metabolism and activity of animals living in the seafloor) is not well constrained. We developed a numerical model to quantify the isotopic signature of benthic DFe fluxes under a wide range of environmental conditions. We find that animal activity promotes the release of more and isotopically heavier iron from the seafloor when bottom-water oxygen concentrations were higher than 50 µM. When oxygen concentrations were lower than 50 µM, animal activity had the inverse effect. Globally, animals living in the seafloor are responsible for an amost threefold increase in iron release from the seafloor. Iron also exhibits more variability in isotopic signatures because of animal activity.

1 Introduction

Iron plays a central role in marine biogeochemical cycles. Over the last 100,000 years, iron has been a limiting micronutrient for marine primary productivity in large parts of the ocean and has been proposed as a driver for glacial-interglacial cycles by modulating atmospheric CO_2 concentrations (Martin, 1990; Watson et al., 2000). Understandably, much work in the past decades has focused on understanding and modelling the oceanic iron cycle (Boyd et al., 2017; Tagliabue et al., 2016, 2017). Yet, many of its aspects still remain poorly constrained, mainly owing to our incomplete understanding of dissolution and scavenging processes (Mahowald et al., 2005; Schroth et al., 2009), as well as to the difficulty of quantifying iron supply from hydrothermal and other sediment sources (Burdige & Komada, 2020; Dale et al., 2015; Elrod et al., 2004; Gartman & Findlay, 2020; Homoky et al., 2016). Continental shelf and slope sediments in particular have been recognised as important contributors to the global iron budget. Sediments can release dissolved iron to the bottom water as reduced ferrous iron (DFe) (Elrod et al., 2004; Severmann et al., 2010) or as particulate iron (oxy)hydroxides (FeOOH) by resuspension of the oxidised surface layer (Burdige & Komada, 2020). The potential DFe flux from continental shelves and slopes is estimated to be ~109 Gmol yr^{-1} (this excludes sources from hydrothermal vents) (Dale et al., 2015), while the global significance of the resuspended particulate flux is currently unknown. It thus exceeds the estimated DFe delivery via rivers (~2.5 Gmol yr^{-1}; Raiswell & Canfield, 2012), glaciers (~0.04 Gmol yr^{-1}; Stevenson et al., 2017), hydrothermal vents (~0.9 Gmol yr^{-1}; Tagliabue et al., 2010), and dust deposition (1-33 Gmol yr^{-1}; Tagliabue et al., 2016). Continental shelf and slope sediments are thus potentially the major source of DFe to the ocean.

The magnitude of the benthic (non-hydrothermal) iron source is modulated by both the amount and reactivity of FeOOH settling on the sediment surface, the organic carbon mineralisation rate in the sediment and bottom-water oxygen concentrations (Dale et al., 2015; Elrod et al., 2004; Lenstra et al., 2018; Pakhomova et al., 2007; Scholz, McManus, et al., 2014; van de Velde, Hylén, et al., 2020). Benthic DFe release is positively correlated with the organic carbon remineralisation rate in the sediment (Elrod et al., 2004; Lenstra et al., 2018) through coupling with dissimilatory reduction of FeOOH (Van Cappellen & Wang, 1995). In contrast, bottom water oxygen concentration negatively correlates with benthic DFe flux (Pakhomova et al., 2007; Severmann et al., 2010) as a result of re-oxidation of DFe to FeOOH (Dale et al., 2015).

If bottom waters turn anoxic and sulphidic, DFe fluxes may eventually decrease again due to the formation of reduced iron sulphide minerals (Pakhomova et al., 2007; Scholz et al., 2014; van de Velde, Hylén, et al., 2020). These biogeochemical controls have recently been quantitatively evaluated in a diagenetic model study (Dale et al., 2015). They found that the relation between the benthic DFe flux (J_{DFe}, units are µmol m^{-2} d^{-1}) and the FeOOH rain rate ($J_{FeOOH,T}$, units are µmol m^{-2} d^{-1} - note that in Dale et al., this was defined as the maximum potential DFe flux away from river mouths), sedimentary organic carbon mineralisation rate (C_{ox}, units are mmol m^{-2} d^{-1}), and bottom-water oxygen concentrations ($[O_2]_{BW}$, units are µM) can be expressed in a transfer function of the form:

$$J_{DFe} = 0.154 J_{FeOOH,T} \tanh\left(\frac{C_{ox}}{[O_2]_{BW}}\right) \quad [1]$$

In this function, bioturbation is not explicitly included but is dependent on $[O_2]_{BW}$, and hence its potential impact on DFe fluxes has not been assessed. However, field observations from estuarine, coastal and shelf sediments have shown that bioturbation exerts an important control on sediment-water DFe fluxes (Elrod et al., 2004; Lenstra et al., 2018; Severmann et al., 2010; Thibault de Chanvalon et al., 2017).

The term bioturbation comprises a variety of animal behaviours, which are grouped into two categories; ‘bio-irrigation’, which describes the transport of dissolved species through animal burrows, and ‘bio-mixing’, which describes the transport of solid-phase particles (Kristensen et al., 2012; Meysman et al., 2006). Both these aspects of bioturbation have contrasting effects on the sedimentary Fe biogeochemistry (van de Velde & Meysman, 2016). Bio-irrigation increases the solute exchange between sediment and water column (Aller, 2001; Aller & Aller, 1998; van de Velde & Meysman, 2016) and local studies in coastal and estuarine sediments have suggested that bio-irrigation increases the benthic DFe flux (Lenstra et al., 2018; Thibault de Chanvalon et al., 2017). Bio-mixing, on the other hand, stimulates Fe cycling within the sediment column (Beam et al., 2018; Canfield et al., 1993; Thamdrup et al., 1994; van de Velde, Hidalgo-Martinez, et al., 2020; van de Velde & Meysman, 2016) and its influence on benthic recycling fluxes tends to be highly dependent on the redox zonation and thus on the complex and dynamic network of biogeochemical processes in marine sediments (Thibault de Chanvalon et al., 2017; van de Velde

& Meysman, 2016). The role of bio-mixing in modulating benthic DFe fluxes on the global scale is largely unknown.

Additionally, no global assessment of the isotopic signature of benthic DFe fluxes, analogous to Eq. [1], exists. However, such a quantification could provide a particularly powerful tool to better constrain marine iron sources and sinks (see, e.g., John et al., 2012). Iron has four stable isotopes (^{54}Fe, ^{56}Fe, ^{57}Fe and ^{58}Fe), of which ^{56}Fe and ^{54}Fe are the most abundant. Accordingly, the ^{56}Fe isotopic signature, calculated as the deviation in ‰ of the ^{56}Fe/^{54}Fe ratio relative to the IRMM−014 reference standard (δ^{56}Fe; Dauphas et al., 2017), is commonly used to constrain the individual sources or sinks of Fe in the ocean (e.g., Conway & John, 2014). For example, particulate iron delivered to the oceans via aerosol deposition or riverine discharge at low latitudes has a δ^{56}Fe signature of ~ 0.0 ‰ (Beard, Johnson, Von Damm, et al., 2003). Dissolved Fe that is released from continental shelves and slopes after reduction of particulate FeOOH in the sediment generally has a light δ^{56}Fe signature of ~ -2.0 ‰ (John et al., 2012; Severmann et al., 2010), whereas iron released following non-reductive dissolution has a δ^{56}Fe of ~ 0.0 ‰ (Homoky et al., 2013). Currently, however, assessment of the magnitude of iron kinetic isotope effects in marine sediments and of the isotopic signature of DFe released from the sediment are scarce. Consequently, our understanding of its response to different environmental conditions, as well as of the δ^{56}Fe signature of the benthic iron source at the global scale is poorly constrained, limiting the accuracy of ocean biogeochemical models (Homoky et al., 2016).

Here, we extend the work of Dale et al. (2015) to address these two major uncertainties in the marine iron cycle; (i) the importance of bioturbation for the global benthic DFe flux, and (ii) the δ^{56}Fe signature of the global benthic DFe flux. First, we combine reaction-transport modelling with previously published field data to determine iron isotope fractionation factors for the most important Fe diagenetic reactions. We then quantify the effect of bioturbation on the benthic DFe flux and its isotopic signature under a range of different bottom-water redox conditions. Finally, we derive two sets of predictive global functions for the magnitude and isotopic signature of the benthic DFe flux based on benthic carbon oxidation rates, bottom-water oxygen concentrations and iron oxide rain rates; (i) for the modern seafloor and (ii) for an unbioturbated seafloor akin to the late Proterozoic seafloor. Ultimately, this work contributes to improve the predictive capacity global ocean biogeochemical models.

2 Materials and Methods

2.1 Approach

Our approach consisted of two separate steps. First, we inversely determined iron isotope fractionation factors for the most pertinent biogeochemical reactions by combining available field data with a site-specific one-dimensional reaction-transport model of marine sediments. The model was applied to two field sites for which solid-phase and pore-water iron concentrations and their isotope values are available ('site-specific model'; Suppl. Text 1). Due to the lack of complete set of field data at the two field sites, the model set-up for the two case studies does not explicitly resolve nitrogen and manganese cycles. However, we contend that the application of a more detailed model for this step would not significantly alter our conclusions.

Informed by these local case studies and based on the 'generic model' used in Dale et al. (2015), we then designed a generic model set-up that explicitely accounts for the entire network of biogeochemical reactions observed in global marine sediments, including nitrogen and manganese ('generic model'; Suppl. Text 2). This generic model set-up is used in a second step consisting of a global sensitivity analysis aimed at assessing the importance of bioturbation and deriving predictive functions linking benthic DFe fluxes and their isotopic signature to their main environmental controls (i.e. C_{ox}, $[O_2]_{BW}$ and $J_{FeOOH,T}$) for both modern bioturbated marine sediments and unbioturbated sediments. These predictive functions are subsequently used to quantify the importance of bioturbation for the global benthic DFe flux, and to assess how future ocean deoxygenation might affect global benthic DFe release.

2.2 Model description

We used a vertically resolved one-dimensional reaction-transport model to simulate the coupled biogeochemical cycles of C, O, N, Mn, Fe and S (C, O, Fe and S in the case of the site-specific model). Solid transport occurs via sediment accumulation and bio-mixing. Solutes are transported by molecular diffusion and bio-irrigation. Bio-mixing is implemented as a diffusion-like process (Meysman et al., 2010), whereas bio-irrigation is described as a non-local exchange process (Boudreau, 1984). The depth-dependent advection velocities of solids and solutes were calculated from the porosity profile and the burial velocities in compacted sediments. The model formulation is informed by previous empirical models (Berg et al., 2003; Bohlen et al., 2011; Van

Cappellen & Wang, 1995; Dale et al., 2015; Meysman et al., 2003; van de Velde, Hidalgo-Martinez, et al., 2020; van de Velde & Meysman, 2016). Suppl. Info. Section 1 and 2 provide a detailed description of the two diagenetic model set-ups. Here, we only briefly discuss the implemented Fe cycle.

The Fe cycle in the generic model (Figure 1) explicitely accounts for four particulate iron oxide fractions that are defined by their reactivity according to wet chemical extraction methods (Canfield et al., 1992; Poulton et al., 2004; Poulton & Canfield, 2005; Raiswell & Canfield, 1998). The most reactive fraction ('highly reactive', FeHR) includes amorphous and reactive crystalline oxides, acid volatile sulphide, pyrite and an ill-defined reduced Fe fraction, which could include adsorbed Fe^{2+} (Poulton, 2003). The half-life of the FeHR fraction is <1 yr. The second most reactive fraction 'moderately reactive' Fe (FeMR) represents more crystalline oxides such as goethite and magnetite, as well as reactive silicates and has a half-life of ~100 years (Poulton et al., 2004). The 'poorly reactive' Fe (FeP) fraction encompasses mostly reactive silicates with a half-life of ~100,000 yrs. The 'unreactive' iron (FeU) fraction includes Fe bound within silicates that do not react on timescales relevant to this study. Only highly reactive iron oxides can be reduced by dissimilatory iron reduction coupled to organic matter mineralisation. Sulphide oxidation on the other hand can reduce highly reactive, moderately reactive and poorly reactive iron oxides. The reduction of iron oxides releases DFe to the pore-water, which can then adsorb on solid-phase particles, be re-oxidised to FeHR or precipitate as iron mono-sulphide (FeS). FeS can be further transformed to pyrite (FeS_2) by reaction with dissolved sulphide or elemental sulphur. More reactive iron classes can age into less reactive fractions. For the site-specific model, we omitted moderately reactive, poorly reactive and unreactive iron mineral classes because of the lack of empirical information with respect to the less reactive iron classes. We did, however, allow the highly reactive class to be comprised of 'fresh' and 'aged' iron oxides, following previous studies (Berg et al., 2003; van de Velde, Hidalgo-Martinez, et al., 2020). Note that in both model set-ups, we do not include non-reductive dissolution of Fe minerals, which is potentially important in sediments characterised by low rates of organic matter mineralisation (Homoky et al., 2013). Non-reductive dissolution is mechanistally not well understood, making it difficult to include it in

diagenetic models. However, because benthic DFe fluxes driven by this dissolution process are very low (~1 µmol m^{-2} d^{-1}), it is likely of minor importance for our study.

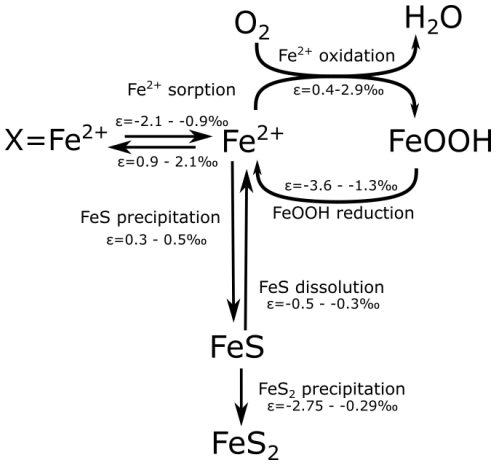

Figure 1: Simplified iron cycle in marine sediments. In the model, iron (oxyhydr)oxides (FeOOH) are modelled as seperate fractions, defined on their reactivity towars sulphide. FeOOH reduction can be coupled to organic matter oxidation or sulphide oxidation. Fe isotope fractionations (ε) are taken from literature and given in parenthesis (Balci et al., 2006; Beard et al., 1999; Beard, Johnson, Skulan, et al., 2003; Bullen et al., 2001; Butler et al., 2005; Crosby et al., 2005, 2007; Guilbaud et al., 2011; Icopini et al., 2004; Johnson et al., 2004; Mansor & Fantle, 2019; Rolison et al., 2018; Welch et al., 2003; Wu et al., 2012).

In addition to total (bulk) Fe, the implemented Fe cycle also tracks ^{56}Fe of all Fe species. To our knowledge, this is the first diagenetic reaction-transport model that simulates iron isotopic signatures of individual Fe species. For simplicity, we assumed that the bulk fraction only consists of the two major Fe isotopes; ^{54}Fe and ^{56}Fe (which constitute > 97% of the total iron pool). Accordingly, the δ^{56}Fe value in dissolved Fe species was calculated as

$$\delta^{56}Fe_{C_i} = \left(\frac{\left({}^{56}C_i \,/ (C_i - {}^{56}C_i \right)}{\left({}^{56}Fe \,/\, {}^{54}Fe \right)_{ref}} - 1.0 \right) x1000 \qquad [2]$$

where C_i represents the concentration of bulk Fe in Fe species *i*, ${}^{56}C_i$ is the concentration of ^{56}Fe in Fe species *i* and $\left({}^{56}Fe \,/\, {}^{54}Fe \right)_{ref}$ is the isotope ratio of a standard sample (15.697861 for IRMM-14; Dauphas et al., 2017). Each individual reaction R_k (which tracks the reaction of the bulk species) has a corresponding isotope-specific reaction ${}^{56}R_k$ that is related to R_k by the fractionation factor ${}^{56}\alpha_{R_k}$

$${}^{56}R_k = \frac{{}^{56}\alpha_{R_k} \, {}^{56}r_{C_i}}{1 + {}^{56}\alpha_{R_k} \, {}^{56}r_{C_i}} R_k \qquad [3]$$

where ${}^{56}r_{C_i}$ represent the $^{56}Fe/^{54}Fe$ isotope ratio of C_i,

$$ {}^{56}r_{C_i} = \frac{{}^{56}C_i}{C_i - {}^{56}C_i} \quad [4] $$

In this study, the fractionation factor ${}^{56}\alpha_{R_k}$ is defined as >1 when the reaction fractionates towards heavier isotopes (the remaining Fe pool becomes lighter), and <1 when the reaction fractionates towards lighter isotopes (the remaining Fe pool becomes heavier). The kinetic isotope effect (${}^{56}\varepsilon_{R_k}$; expressed in ‰), was then calculated from ${}^{56}\alpha_{R_k}$ as,

$$ {}^{56}\varepsilon_{R_k} = 1000({}^{56}\alpha_{R_k} - 1) \quad [5] $$

To avoid extreme $\delta^{56}Fe$ values at low bulk concentrations, a fractionation limit ($C_{\lim}$) was set at 10^{-9} µmol cm^{-3} of sediment. Reactions that proceeded below this bulk concentration induced no fractionation,

$$ {}^{56}R_k[C_i < C_{\lim}] = \frac{{}^{56}C_i}{C_i} R_k \quad [6] $$

Adsorption of ferrous iron to clay or oxide minerals (Poulton, 2003) was modelled as an instantaneous equilibrium (Berg et al., 2003),

$$ [X \equiv Fe^{2+}] = K_{ads}^{Fe^{2+}} [Fe^{2+}] \quad [7] $$

where $K_{ads}^{Fe^{2+}}$ is a dimensionless adsorption constant (Berg et al., 2003). To account for isotope fractionation during adsorption, the pool of adsorbed ^{56}Fe was calculated as,

$$ \left[X \equiv {}^{56}Fe^{2+}\right] = K_{ads}^{Fe^{2+}} \frac{{}^{56}\alpha_{FIS} + {}^{56}\alpha_{FIS}\,{}^{56}r_{Fe^{2+}}}{1 + {}^{56}\alpha_{FIS}\,{}^{56}r_{Fe^{2+}}} \left[{}^{56}Fe^{2+}\right] \quad [8] $$

where ${}^{56}\alpha_{FIS}$ is the fractionation factor associated with ferrous iron sorption, and all other parameters have been defined previously. The model was implemented in the open-source programming language R (R Core Team, 2017), following the procedures of Soetaert and Meysman (2012). Please refer to the Suppl. Information for further information about the model implementation, parametrisation (Table 1 and Table 2) and solution.

Table 1: List of boundary conditions and parameters used in the reaction-transport model used for calibration of the isotope fractionation factors. Solid-phase concentrations are expressed per unit volume of solid phase. "Method" refers to the procedure by which parameter values are constrained: A = Literature values, B = model calibration. Note that all isotope values are given relative to the IRMM-14 standard. MC=Moneterey Canyon, SBB=Santa Barbara Basin.
References: [1] Reimers et al. (1996), [2] Meysman et al. (2005), [3] Severmann et al. (2006), [4] Dauphas et al., (2017)

ENVIRONMENTAL PARAMETERS	**Symbol**	**Value**		**Units**	**Method**	**References**
		SBB	**MC**			
Temperature	T	10	10	ºC	A	[1],[2]
Salinity	S	34.2	34.2	-	A	[1],[2]
Porosity (surface value)	ϕ_F^0	0.948	0.948	-	A	[1],[2]
Porosity (asymptotic at depth)	ϕ_F^∞	0.824	0.824	-	A	[1],[2]
Porosity attenuation coefficient	x_ϕ	3.6	3.6	cm	A	[1],[2]
Solid-phase density	ρ_S	2.6	2.6	g cm^{-3}	A	[1],[2]
Burial velocity in compacted sediment	v_S, v_F	250	250	cm kyr^{-1}	A	[3]
Bio-mixing depth	z_L	0	10	cm	B	
Biodiffusion coefficient	$D_{b,0}$	0	20	cm^2 yr^{-1}	B	
Bio-irrigation coefficient	α_0	0	183	yr^{-1}	B	
Bio-irrigation attenuation coefficient	x_{irr}	0	3	cm	B	
Depth of sediment domain	L	150	150	cm	-	
$^{56}Fe/^{54}Fe$ isotope ratio of IRMM014	-	15.697861		-	A	[4]
BOUNDARY CONDITIONS	**Symbol**	**Value**		**Units**	**Method**	**References**
Oxygen bottom water	$[O_2]$	0.01	0.28	mol m^{-3}	A	[1]-[3]
Sulphate bottom water	$[SO_4^{2-}]$	28.0	28.0	mol m^{-3}	A	[1]-[3]
DIC bottom water	$\sum CO_2$	2.45	2.45	mol m^{-3}	A	[1],[2]
Ferrous iron bottom water	[DFe]	0	0	mol m^{-3}	A	[1],[2]
Free sulphide bottom water	$[HS^-]$	0	0	mol m^{-3}	A	[1],[2]
Methane bottom water	$[CH_4]$	0	0	mol m^{-3}	A	[1],[2]
Flux POC	J_{POC}	4.6	8.0	mmol m^{-2} d^{-1}	B	
Flux $FeOOH_T$	$J_{FeOOH,T}$	0.56	0.32	mmol m^{-2} d^{-1}	B	
Isotopic signature of $FeOOH_T$	$\delta^{56}Fe_{FeOOH}$	-1.5	-0.5	‰	B	
Flux FeS	J_{FeS}	0	0	mmol m^{-2} d^{-1}	B	
Isotopic signature of FeS	$\delta^{56}Fe_{FeS}$	-	-	‰	B	
Flux FeS_2	J_{FeS2}	0.03	0.03	mmol m^{-2} d^{-1}	B	
Isotopic signature of FeS_2	$\delta^{56}Fe_{FeS2}$	-0.4	0.0	‰	B	

2.3 Determination of Fe isotope fractionation factors

The site-specific model set-up used for the determination of iron isotope fractionation factors resolves the biogeochemical cycling of all chemical species that can be constrained by field data (i.e. FeOOH, FeS, FeS_2 and DFe) in the upper 150 cm of the sediment column. We used the

dataset from sites in Monterey Canyon and Santa Barbara Basin (Severmann et al., 2006). The data sets comprise concentrations of pore-water Fe and Fe-bearing minerals and their respective $\delta^{56}Fe$ values. It includes two contrasting sites; a bioturbated site underlying a fully oxygenated water column (Monterey Canyon), and an unbioturbated site underlying a hypoxic (<10 µM O_2) water column (Santa Barbara Basin) (Table 1; Severmann et al., 2006). We first fitted the bulk concentrations of dissolved Fe (DFe), HCl-extractable Fe (Fe_{HCl}) (which includes FeOOH, sorbed Fe^{2+} and FeS) and pyrite (FeS_2). Subsequently, the isotope fractionations were determined by finding the best model data fit to the $\delta^{56}Fe$ signature of the three distinct Fe pools. Site-specific boundary conditions were constrained on the basis of observational data and are provided in Table 1.

2.4 Model sensitivity experiments: Assessing the role of bioturbation and deriving predictive functions

All sensitivity experiments described below were performed using the generic model. A detailed description of the set-up is provided in Suppl. Info. Section 2. The boundary conditions and bioturbation parameters of the baseline simulation were chosen to represent a generic shelf sediment, and all parameter values were selected from compiled datasets or previously published studies (Table 2; following Dale et al., 2015). Fractionation factors for each iron reaction were constrained based on the derived isotope fractionation factors from the local case studies and compared to literature values (Section 3.1 and Table 4).

Five model sensitivity experiments were designed to investigate the effect of bioturbation on the magnitude and isotopic signature of the benthic DFe flux:

- 'Baseline': both bio-mixing and bio-irrigation were dependent on bottom water oxygen concentrations (Table 2).
- 'Unbioturbated': bio-mixing and bio-irrigation parameters were set to zero
- 'Always bioturbated': bio-mixing and bio-irrigation parameters were set to their maximum value ($D_{b,0}$=10 cm^2 yr^{-1}, z_L=9.7 cm, α_0=290 yr^{-1}; Table 2) and independent of oxygen concentrations.

- 'Only bio-mixing': bio-mixing parameters were set at their maximum value ($D_{b,0}$=10 cm^2 yr^{-1}, z_L=9.7 cm; Table 2) and independent of bottom water oxygen concentrations and bio-irrigation parameters were set to zero.
- 'Only bio-irrigation': bio-mixing parameters were set to zero and bio-irrigation were set at their maximum value (α_0=290 yr^{-1}; Table 2) and independent of bottom water oxygen concentrations

For each of the five experiment, bottom water oxygen concentrations were varied between 1 and 200 µM. The remaining boundary conditions were set to their baseline values (Table 2). In addition, we ran two sets of extended sensitivity experiments to derive a mathematical expression for the magnitude and isotopic signature of the benthic DFe flux as a function of C_{ox}, $[O_2]_{BW}$ and $J_{FeOOH,T}$:

- 'modern seafloor': bio-mixing and bio-irrigation parameters were dependent on bottom water oxygen concentrations based on the relationship proposed by Dale et al. (2015) (Table 2). POC rain rate (J_{POC}, which determined C_{ox} – see Table 2) and bottom-water oxygen concentrations ($[O_2]_{BW}$) were varied across the range typically observed in shelf and slope bottom waters, i.e. 0.5 and 16 mmol C m^{-2} d^{-1} and 1 and 200 µM O_2, respectively (Table 2; Dale et al., 2015). We consecutively ran the same sensitivity experiment with varying J_{POC} and $[O_2]_{BW}$ for a range of plausible total FeOOH ($FeOOH_T$) fluxes (194 to 1914 µmol Fe m^{-2} d^{-1}; Table 2).
- 'Unbioturbated seafloor': bio-mixing and bio-irrigation parameters were set to zero, and we tested the same ranges of environmental conditions described above. In addition, to varying FeOOH fluxes, we also ran the model over a range of sulphate concentrations between 0 and 28 mM to test the potential influence of lower sulphate concentrations, as observed throughout Earth's history (Wortmann & Paytan, 2012).

Table 2: Boundary conditions for the baseline simulation (generic model). Invariable parameters across all simulations are given in the Supplementary Information. All isotope values are given relative to the IRMM-14 standard.

BOUNDARY CONDITIONS	**Symbol**	**Baseline value**	**Sensitivity analysis**	**Units**
Characteristic water depth [a]	-	350	350	m
Temperature [b]	T	10	10	°C
Sediment accumulation rate at infinite depth [c]	v_S, v_F	60	60	cm kyr^{-1}
Oxygen bottom water	$[O_2]_{BW}$	120	1-200 [d]	µM
Sulphate bottom water	$[SO_4^{2-}]_{BW}$	28	0-28 [e]	mM
Ferrous iron bottom water	$[DFe]_{BW}$	0	0	µM
Isotopic signature	$\delta^{56}Fe_{DFe}$	-	-	‰
POC rain rate [f]	J_{POC}	10	0.5-16 [g]	mmol m^{-2} d^{-1}
Flux $FeOOH_T$ [h]	$J_{FeOOH,T}$	1110	194-1914 [i]	µmol m^{-2} d^{-1}
Isotopic signature of $FeOOH_T$	$\delta^{56}Fe_{FeOOH,T}$	0.0	0.0	‰
Flux FeS	J_{FeS}	0.0	0.0	µmol m^{-2} d^{-1}
Isotopic signature of FeS	$\delta^{56}Fe_{FeS}$	-	-	‰
Flux FeS_2	J_{FeS2}	0.0	0.0	µmol m^{-2} d^{-1}
Isotopic signature of FeS_2	$\delta^{56}Fe_{FeS2}$	-	-	‰
BIOTURBATION PARAMETERS				
Bio-diffusion coefficient [j,k]	$D_{b,0}$	$10.f$	variable	cm^2 yr^{-1}
Mixing depth [l]	z_L	$z_L = 1.0 + 9.0 \times (1 - e^{-D_{b,0}/3.0})$	variable	cm
Bio-irrigation coefficient [j,m,n]	α_0	$290.f$	variable	yr^{-1}

[a] (Menard & Smith, 1966) [b] (Thullner et al., 2009) [c] (Burwicz et al., 2011)
[d] Tested values were 1, 2, 5, 10, 15, 25, 50, 100, 120 and 200 µM.
[e] Only tested for the 'Unbioturbated seafloor' experiment. Tested values were 0, 0.01, 0.1, 1 and 28 mM.
[f] Estimated mean carbon oxidation rate for sediments < 200m water depth by Burdige (2007).
[g] Tested values were 0.5, 1, 2, 4 ,6, 8, 10, 12, 14 and 16 mmol C m^{-2} d^{-1}, which gives carbon oxidation rates of 0.4, 0.8, 1.6, 3.3, 4.9, 6.6, 8.3, 9.9, 11.6, and 13.2 mmol C m^{-2} d^{-1} (the remaining POC fraction is buried below the model domain).
[h] Flux value of total iron oxides for the standard model of Dale et al. (2015), 50% of this flux is considered unreactive (Poulton & Raiswell, 2002), and the other 50% is divided equally among FeHR, FeMR, and FePR (Dale et al., 2015).
[i] Tested values were: 194, 278, 555, 1110 and 1914 µmol m^{-2} d^{-1}.
[j] Mean bio-diffusion coefficient of the modern data compilation of Solan et al. (2019).
[k] f represents a dimensionless factor that scales bio-mixing and bio-irrigation coefficients to bottom water oxygen (as introduced by Dale et al., 2015). f equals $0.5 + 0.5erf\left(([O_2]_{BW} - a)/b\right)$ where a = 20 µM and b=12 µM (Dale et al., 2015).
[l] Mixing depth is calculated from the bio-diffusion coefficient as $z_L = 1.0 + 9.0 \times (1 - e^{-D_{b,0}/3.0})$ as introduced previously by van de Velde and Meysman (2016) (see Supplementary Information).
[m] Following Meile et al. (2005) and Dale et al. (2015), the solute-specific Fe^{2+} bio-irrigation parameter is 20% of the bio-irrigation coefficient, and the solute-specific HS^- bio-irrigation coefficient is 50% of the bio-irrigation coefficient.
[n] The attenuation coefficient of bio-irrigation is kept constant at 1.4 cm during the sensitivity analysis.

2.5 Quantifying the importance of bioturbation and environmental change for the global benthic DFe flux

The predictive functions were subsequently used to derive a global estimate of the benthic DFe flux and its $\delta^{56}Fe$ signature for the modern seafloor and a seafloor without any bioturbation. We used $[O_2]_{BW}$ from World Ocean Atlas 2018 on a 1°x1° resolution (available at https://www.nodc.noaa.gov/OC5/woa18/). We then combined this with estimated C_{ox} rates for each of the bathymetric intervals (Burdige, 2007). Because no information about the spatial

distribution of FeOOH fluxes is currently available, we assumed a globally uniform $F_{FeOOH,T}$ of 1110 µmol m^{-2} d^{-1}, to be consistent with previous work (Dale et al., 2015). We calculated the mean and total DFe flux (J_{DFe}) for several water depth intervals, as well as the mean $\delta^{56}Fe$ signature of the DFe flux. Finally, to assess the impact of decreasing $[O_2]_{BW}$ on DFe release from the seafloor, we decreased $[O_2]_{BW}$ retrieved from the World Ocean Atlas 2018 (see section 3.4), by 5, 10, 20 and 40 µM, keeping all other input constant. These decreases in $[O_2]$ are broadly consistent with Earth System models predictions of a globally averaged decrease of ~15 µM O_2 in the ocean, with local maxima up to a 45 µM decrease (Kwiatkowski et al., 2020).

3 Results and discussion

3.1 Determination of iron isotope fractionation factors

Figure 1a-b illustrates the best fit simulations for the fitted iron isotope fractionantion factors. For the **Monterey Canyon** (MC) sediment, the model provided a good fit to the measured bulk Fe-mineral distributions and pore-water DFe concentrations (Figure 1a-b). Modelled DFe concentrations slightly underpredict measured concentrations (Figure 1b), whereas the modelled benthic flux was ~27% higher to measured benthic fluxes from nearby locations (note that the measured fluxes are not from the same location nor the same sampling time as the sediment data) (Table 3). Overall, the model was able to capture the major features of MC iron geochemistry, such as the persistence of reactive iron oxides and DFe with depth, and only a limited accumulation of FeS_2, well (Figure 1). For the **Santa Barbara basin** (SBB) sediment, the model predicted the measured Fe-mineral distributions, the depletion depth of DFe and the benthic DFe flux correctly (Figure 1f-g, Table 3). However, it does not reproduce well the DFe peak (Figure 1g). It is possible that the rate of sulphate reduction in the upper sedimentary layers is overestimated, which would lead to precipitation of DFe as FeS. However, reducing sulphate reduction allows DFe to persist beyond 30 cm, which is also at odds at the data. Nevertheless, this mismatch does not affect the benthic flux, as this is determined by the DFe gradient near the SWI, which is comparable between model and data, as shown by the estimated benthic flux (Table 3). Furthermore, it should be noted that pore water and solid phase biogeochemistry operate on different time scales (solid phase generally integrates the last 100 years, whereas pore water responds to seasonal changes). We chose to put more weight on the solid phases, as this provides a long-term biogeochemical view at the field sites.

Table 3: Study sites and comparison of geochemical data with the model output of the sites used for initial model calibration.

Name	Latitude Longitude	Water depth (m)	Bottom water O_2 (µM)		Carbon oxidation rate (mmol m^{-2} d^{-1})		Benthic DFe flux (µmol m^{-2} d^{-1})		δ^{56}Fe-DFe of benthic flux (‰)	
			Data	*Model*	*Data*	*Model*	*Data*	*Model*	*Data*	*Model*
Monterey Canyon (MC)	36º 47.67' N 121º 53.65' W	450	>100[a]	280	6-17[a]	7.06	1.1-15[a]	19	-2.7 ± 1.1[d]	-1.3
Santa Barbara Basin (SBB)	34º 16.87' N 119º 54.84' W	496	~10[b]	10	<4[b]	3.85	>331[c]	248	-3.6 ± 0.7[c]	-2.9

[a] Data from Berelson et al. (2003). Note that these fluxes are for a nearby site at a shallower depth and thus not the same site as where the sediment data was collected.
[b] From Meysman et al. (2003), based on data from Reimers et al. (1996) which is from the deepest point of the SBB. Pore-water ammonium and sulphate profiles suggest that the carbon oxidation rate is lower at 496 m depth.
[c] Data for the California margin and Borderland Basins from Severmann et al. (2010) at nearby sites.
[d] Data for the Eel River Shelf and Umpqua River Shelf from Severmann et al. (2010), which are comparable sites to the Monterey Canyon site (bioturbated and oxygenated water column). Isotope values are only shown for reference, and the model has not been calibrated to these values.

The best fit δ^{56}Fe-DFe profile for the **Monterey Canyon** sediment tracked the measured profile remarkably close, increasing from a low value of ~ -3.0 ‰ at the sediment surface and peaking at ~ -1.0 ‰ at 5cm depth, followed by a decrease and stabilisation at around -1.5 ‰ (Figure 1d). Consistent with the measured data, there was very little downcore variation in modelled δ^{56}Fe-Fe_{HCl} (-0.5 ‰), although the model did not reproduce the very low -0.9 ‰ near the sediment-water interface (Figure 1c). This model-data misfit does not affect the overall δ^{56}Fe-DFe pattern (which is the focus of this study). The measured δ^{56}Fe-FeS_2 profile showed a significant amount of scattering in the upper sedimentary layers, but the general decrease from ~ -0.5 ‰ near the SWI to ~ -0.8 ‰ at 50 cm depth is broadly reproduced by the model (Figure 1e). The concentration of FeS_2 was very low in the MC sediment (Figure 1e), and could have been influenced by a (variable) detrital input, which is not included in our model. These uncertainties directly translate into the fractionation factor for pyrite precipitation fitted for the MC sediment, which thus remains uncertain (see below).

For the **Santa Barbara basin**, the model reproduced the measured δ^{56}Fe-DFe data very well, starting slightly more negative at the sediment surface, and reaching up to +1 ‰ at around 15 cm depth (Figure 1i). The modelled δ^{56}Fe-Fe_{HCl} profile showed a rapid increase near the SWI (Figure 1h), driven by the loss of isotopically light iron during dissimilatory iron reduction, which is subsequently released to the overlying water column as a benthic flux, consistent with observations (Table 3). The modelled δ^{56}Fe-Fe_{HCl} profiles showed a gradual increase with depth with a similar gradient as the measured profile, but with a slight offset of ~0.3 ‰ (Figure 1h). The

modelled δ^{56}Fe-FeS_2 profile followed the initial decrease in the measured δ^{56}Fe-FeS_2 profile well, but with an increase toward the bottom of the core (Figure 1j). This mismatch is likely caused by a slight overestimation of the pyrite precipitation rate at depth (Figure 1f).

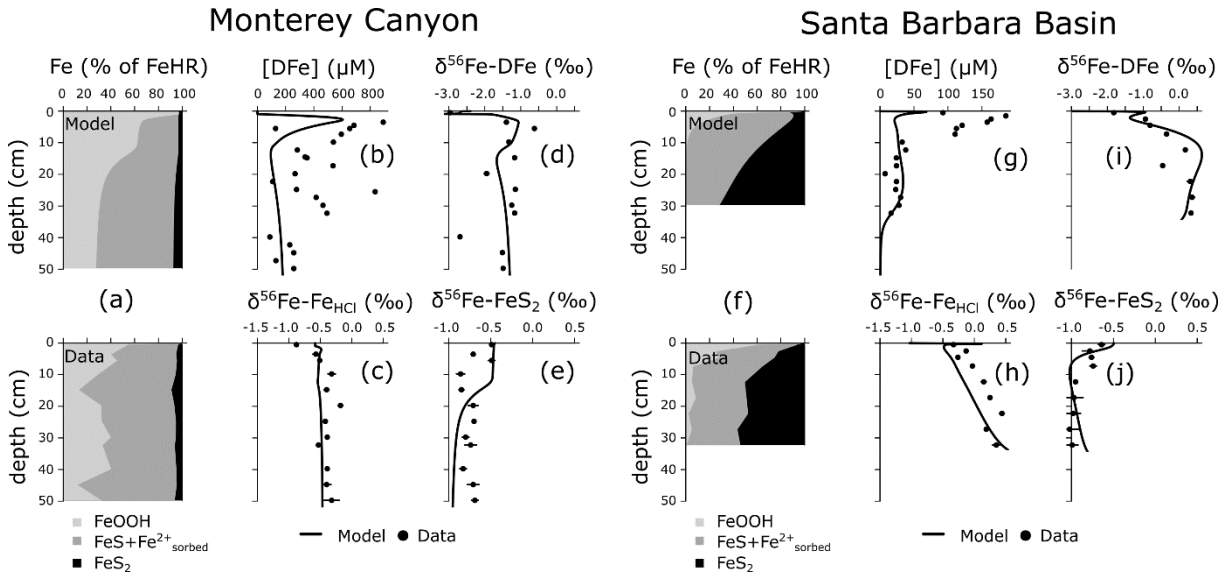

Figure 2: Model fit to the data from Monterey Canyon and Santa Barbara Basin (Severmann et al., 2006). Monterey Canyon: (a) Modelled and measured fractions of highly reactive iron minerals (FeHR). (b) Dissolved Fe (DFe) concentrations. δ^{56}Fe compositions of (c) HCl-extractable Fe minerals (δ^{56}Fe-Fe_{HCl}), (d) dissolved Fe (δ^{56}Fe-DFe), (e) pyrite (δ^{56}Fe-FeS_2). Santa Barbara Basin: (f) Modelled and measured fractions of highly reactive iron minerals (FeHR). (g) Dissolved Fe (DFe) concentrations. δ^{56}Fe compositions of (h) HCl-extractable Fe minerals (δ^{56}Fe-Fe_{HCl}), (i) dissolved Fe (δ^{56}Fe-DFe), (j) pyrite (δ^{56}Fe-FeS_2). Note that δ^{56}Fe values are reported vs. igneous rock, to allow direct comparison with the data of Severmann et al. (2006). On this scale, the δ^{56}Fe value of the IRMM-14 standard (which is the notation used in the rest of this manuscript) is -0.09‰ (Beard, Johnson, Skulan, et al., 2003).

Overall, the diagenetic model was able to capture the important trends in bulk concentration and isotopic signatures throughout the sediment column of two very different field sites (Figure 1). Furthermore, it was able to simulate the expected magnitude and isotopic composition of the benthic DFe flux (Table 3). More importantly, the observed trends could be reproduced by applying the same fractionation factors and almost all such derived fractionation factors are consistent with literature values (Table 4). Yet, the fractionation factor for FeS_2 precipitation is an exception. Model fitting resulted in different fractionation factors at each site; -0.4 ‰ and -0.7‰ (Table 4). These compare well to -0.78 ± 0.15 ‰ previously derived from the same data by Severmann et al. (2006), and the value of -0.51 ± 0.22 ‰ obtained by Mansor & Fantle (2019) in laboratory experiments. We are more confident in the fractionation factor obtained from the SBB sediments (see above), and therefore, we here apply an isotope effect of -0.7 ‰ for pyrite precipitation that is also fully consistent with previous field observations (Severmann et al.,

2006). The ensemble of derived fractionation factors summarised in Table 4 is used to inform the parametrisation of the generic model set-up in the sensitivity studies (Suppl. Info. Section 2).

Table 4: Modelled fractionation factors compared to *in situ* and laboratory values reported in the literature. These were used in the numerical sensitivity experiment. For pyrite precipitation, we selected -0.7 ‰, as this value is consistent with previous field observations (Severmann et al., 2006).

Reaction	Reactant	Product	Fractionation factor ($^{56}\varepsilon_{R_k}$)		References
			Model	Literature range	
Dissimilatory iron reduction[a]	FeOOH	DFe	-1.3 ‰	-3.6 ‰ to -1.3 ‰	[1]-[5]
Ferrous iron oxidation[b]	DFe/FeS/FeS_2	FeOOH	+0.4 ‰	+0.4‰ to +2.9‰	[6]-[8]
Ferrous iron adsorption	DFe	X=DFe	+0.4 ‰	-0.9 ‰ to +2.1 ‰	[3],[9],[10]
Iron sulphide precipitation	DFe	FeS	+0.5 ‰	+0.3 ‰ to +0.5 ‰	[11],[12]
Iron sulphide dissolution	FeS	DFe	-0.5 ‰	-0.5 ‰ to -0.3 ‰	[11],[12]
Pyrite precipitation	FeS	FeS_2	-0.4 ‰ (MC) -0.7 ‰ (SBB)	-2.75 ‰ to -0.29 ‰	[6],[13],[14]

[1] (Beard et al., 1999) [2] (Beard, Johnson, Skulan, et al., 2003) [3] (Crosby et al., 2005) [4] (Welch et al., 2003) [5] (Crosby et al., 2007) [6] (Rolison et al., 2018) [7] (Bullen et al., 2001) [8] (Balci et al., 2006) [9] (Johnson et al., 2004) [10] (Icopini et al., 2004) [11] (Wu et al., 2012) [12] (Butler et al., 2005) [13] (Guilbaud et al., 2011) [14] (Mansor & Fantle, 2019)

[a] DIR coupled to organic matter mineralisation and sulphide oxidation are assigned the same fractionation factor

[b] All oxidation reactions (i.e. iron sulphide oxidation and pyrite oxidation) are assigned the same fractionation factor

3.2 Effect of bioturbation on the benthic iron flux and its isotopic signature under different bottom water redox conditions

The results of the five bioturbation activity scenarios (section 2.4) under a range of plausible environmental conditions highlights the importance of dynamic interplay between oxygen and macrobenthic activity on benthic iron fluxes and their isotopic signature.

3.2.1 Magnitude of the benthic iron flux

For unbioturbated sediments, the DFe flux (J_{DFe}) rapidly decreases from > 150 µmol m^{-2} d^{-1} to < 50 µmol with increasing $[O_2]_{BW}$ and then become essentially zero at $[O_2]_{BW}$ > 50 µM (Figure 2a). At low $[O_2]_{BW}$, the oxygen penetration depth OPD is shallow and, as a consequence, most Fe redox cycling is concentrated near the SWI supporting higher DFe fluxes out of the sediment (Figure 3a). More importantly, low O_2 concentrations result in an inefficient oxidation of the reduced DFe, thus allowing a significant fraction of the flux to escape the sediment (Figure 2a). An increase in $[O_2]_{BW}$ stimulates benthic Fe cycling and provides a more efficient re-oxidation barrier for the DFe flux (Figure 3a). As a consequence, decreasing J_{DFe} is observed with an increase

in the integrated production rate of DFe (P_{DFe}, which is a proxy for the intensity of the Fe redox cycle; Canfield et al., 1993; van de Velde & Meysman, 2016) (Figure 2a,e).

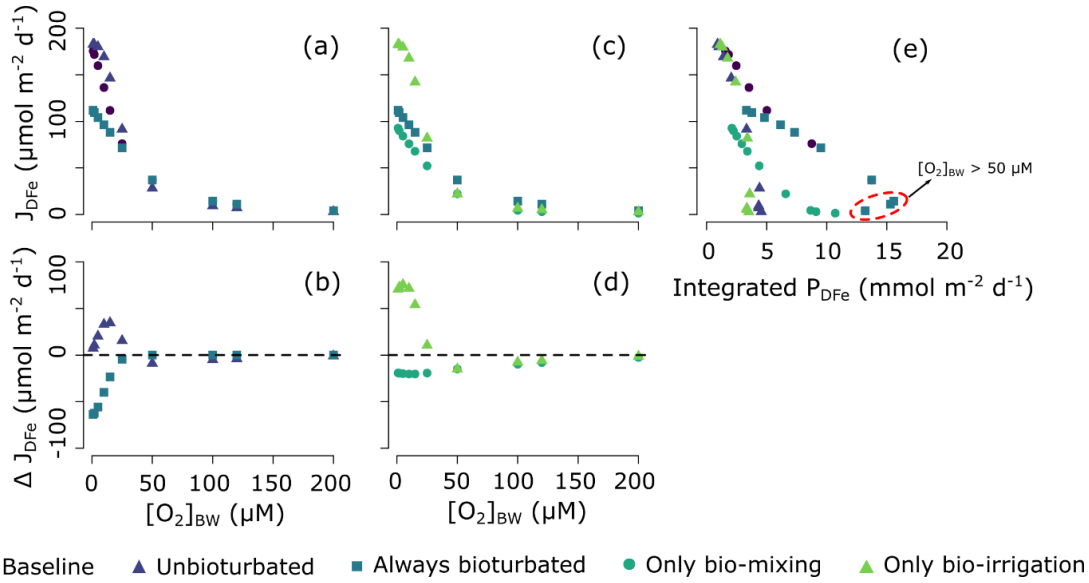

Figure 3: (a)-(d) Effect of bioturbation on the magnitude (J_{DFe}) of the benthic DFe flux for different bottom water oxygen concentrations using the generic model. Data in panel (b) are calculated as the difference between the 'always bioturbated' (or 'unbioturbated') run and the 'baseline' run, data in panel (d) are calculated as the difference between the 'only bio-mixing' (or 'only bio-irrigation') run and the 'always bioturbated' run. (e) magnitude of the benthic DFe flux plotted against the integrated production rate of DFe (P_{DFe}), which is a proxy for the intensity of the Fe redox cycle (see Canfield et al., 1993; van de Velde & Meysman, 2016).

Bioturbated sediments reveal a similar overall decrease in J_{DFe} with increasing $[O_2]_{BW}$ (Figure 2a). However, the presence of bioturbating fauna attenuates the high DFe fluxes simulated at low $[O_2]_{BW}$ (<50 µM), while it slightly amplifies the very low DFe fluxes simulated for higher $[O_2]_{BW}$ conditions (Figure 2a,b). Results thus indicate that the effect of bioturbation on J_{DFe} is dependent on $[O_2]_{BW}$. At low $[O_2]_{BW}$, bio-mixing drives a decrease in J_{DFe} relative to the unbioturbated sediment (Figure 2b). Although bio-mixing directly enhances the total production of reduced DFe in the sediment by mixing both organic matter and iron oxides deeper down in the sediments (Figure 3a,c), it also stimulates the consumption of this DFe via precipitation or reoxidation reactions (Berner & Westrich, 1985; van de Velde & Meysman, 2016). Bio-mixing moves Fe cycling away from the SWI, which increase diffusional distance to the sediment surface, and allows most of the DFe to be re-oxidised or precipitated as iron sulphide minerals (Figure 3a,c). This is reflected in the decrease of J_{DFe} with an increase in sedimentary Fe redox cycling (Figure 2e). The positive effect of bioturbation on J_{DFe} fluxes at higher $[O_2]_{BW}$ is only observed when both bio-mixing and bio-irrigation work in concert. This is because bio-mixing is required

to stimulate Fe cycling and build-up pore-water DFe concentrations, while bio-irrigation efficiently transports DFe out of the sediment (Figure 3c,d). Hence, while the individual effects of biomixing and irrigation affect the sediment biogeochemistry in different ways, both mixing and irrigation contribute to increasing J_{DFe} under normal oxic bottom waters.

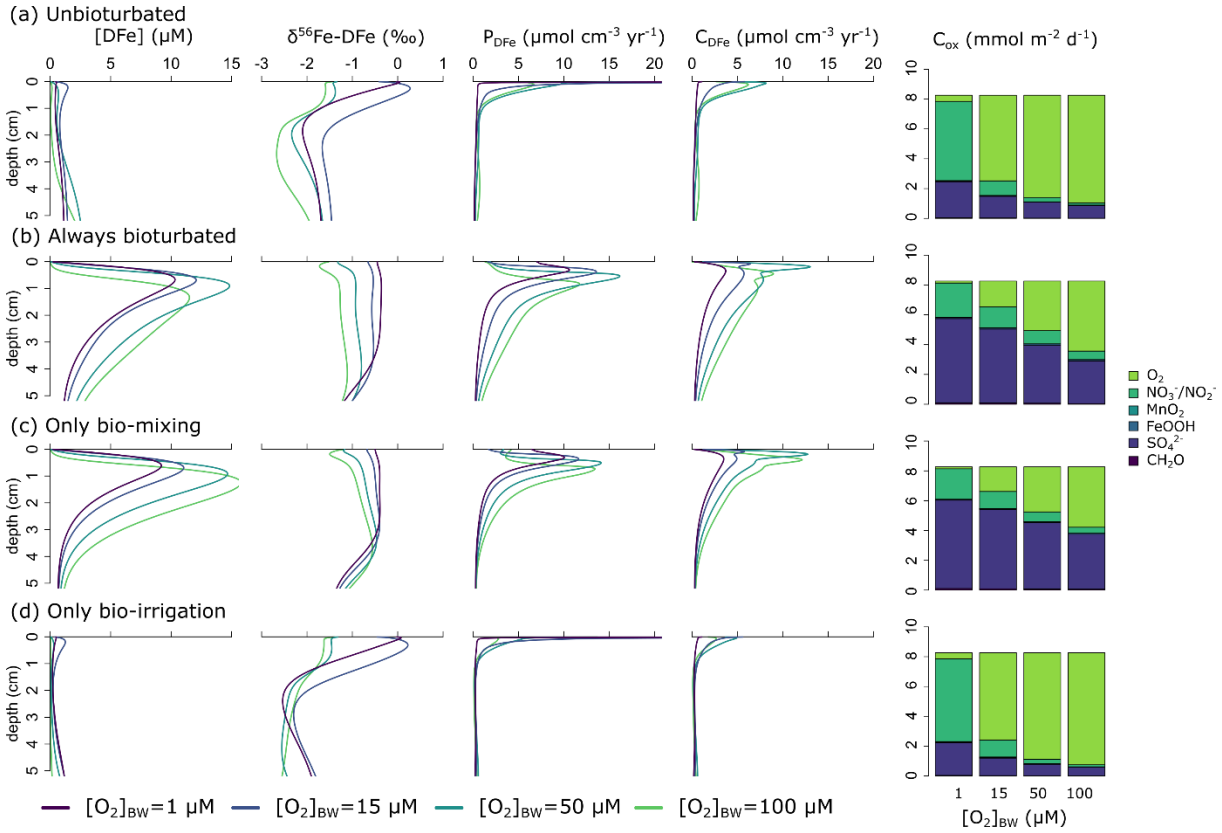

Figure 4: Vertical diagenetic profiles of dissolved iron concentrations ([DFe]), δ^{56}Fe signature of DFe (δ^{56}Fe-DFe), total ferrous iron production rate (P_{DFe}), total ferrous iron consumption rate (C_{DFe}) for different bottom water oxygen concentrations and partitioning of the individual mineralisation pathways. Manganese oxide reduction, iron oxide reduction and methanogenesis are not visible on this scale. (a) bioturbation is set to zero. (b) bioturbation is independent of oxygen concentrations and always at its maximum (see Table 2). (c) only bio-mixing is turned on and independent of oxygen concentrations. (d) only bio-irrigation is turned on and independent of oxygen concentrations.

3.2.2 Isotopic signature of the benthic iron flux

The isotopic signature of the benthic DFe flux is affected by the magnitude of J_{DFe} and rate of FeS_2 burial (Figure 4). As discussed in the previous section, these processes are affected by $[O_2]_{BW}$ and bioturbation, which will thus also exert a control on δ^{56}Fe-J_{DFe}.

The relationship between the magnitude and the isotopic signature of J_{DFe} is partly driven by a Rayleigh distillation effect due to the semi-open nature of aquatic sediments (Jorgensen,

1979). Benthic DFe is derived from the reduction of the finite FeOOH deposition flux and can escape the sediment as a benthic return flux. Hence, as more DFe escapes the sediment through the sediment-water interface, less FeOOH remains. For example, we here apply a $FeOOH_T$ flux of 1110 µmol Fe m^{-2} d^{-1} with an isotopic composition of 0.0 ‰ (Table 2). Of this deposition flux, at most ~15% (or ~170 µmol Fe m^{-2} d^{-1}; Eq. [1]) is released from the sediment column). As FeOOH is reduced and escapes the sediment as DFe, both the remaining FeOOH pool, and thus also the produced DFe, become isotopically heavier (i.e. shift to higher δ^{56}Fe values; Figure 4e). As a consequence, a positive relation between δ^{56}Fe-J_{DFe} and the magnitude of J_{DFe} is observed (Figure 4e). If we assume no redox cycling of Fe (i.e. all DFe released from the sediment is derived from FeOOH with a fractionation factor of -1.3 ‰; Table 4) and 170 µmol Fe m^{-2} d^{-1} is the maximum amount of DFe that can be released, we can calculate the expected δ^{56}Fe-J_{DFe} as a Rayleigh fractionation curve (Figure 4e). The unbioturbated and bio-irrigated model show lighter values than expected for J_{DFe} < 50 µmol Fe m^{-2} d^{-1}, indicating partial re-oxidation (which makes the DFe pool lighter; Table 4). At higher J_{DFe}, both unbioturbated and bio-irrigated model runs more closely follow a typical Rayleigh fractionation (Figure 4e). In contrast, the results of the bio-mixing model run plot consistently above the Rayleigh fractionation line (thus showing heavier δ^{56}Fe values than expected). By stimulating sulphate reduction (Figure 3c), bio-mixing increases FeS_2 precipitation and burial (Figure 4f). Because fractionation during FeS_2 precipitation is negative (i.e., FeS_2 is lighter than the FeS it is formed from), this constitutes a sink of light Fe (Figure 4g), which leads to a heavier isotopic signature of the benthic DFe flux (Figure 4e). When both bio-mixing and bio-irrigation are active, Fe redox cycling is enhanced relative to the only bio-mixing or only bio-irrigation runs (Figure 2e). At the same time, enhanced availability of O_2 due to burrow flushing limits FeS_2 burial (Figure 2f), leading to a lighter isotopic signature of the benthic DFe flux (Figure 4e). At higher J_{DFe} (and thus lower $[O_2]_{BW}$; Figure 2), FeS_2 burial is enhanced, leading to heavier δ^{56}Fe values than expected (Figure 4e,f).

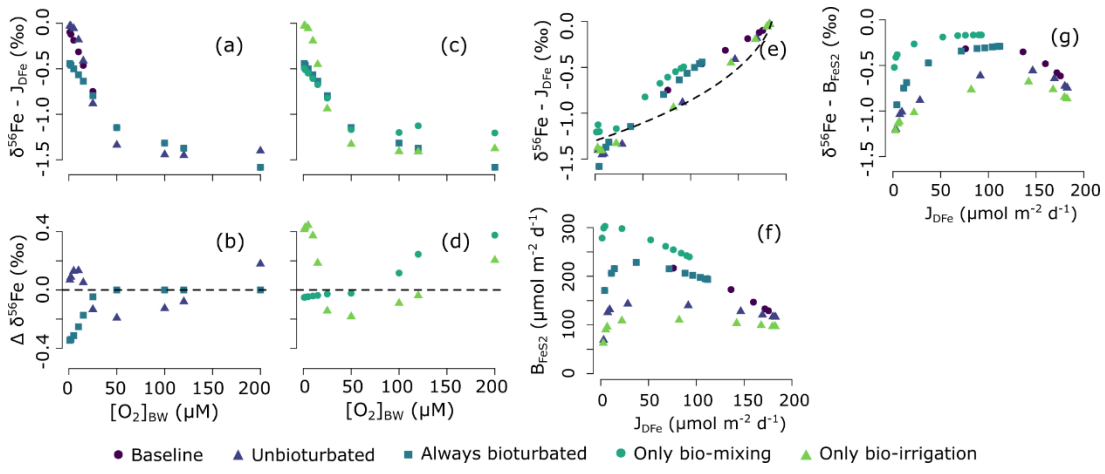

Figure 5: (a)-(d) Effect of bioturbation on the δ^{56}Fe signature (δ^{56}Fe-J_{DFe}) of the benthic DFe flux for different bottom water oxygen concentrations using the generic model. Data in panel (b) are calculated as the difference between the 'always bioturbated' (or 'unbioturbated') run and the 'baseline' run, data in panel (d) are calculated as the difference between the 'only bio-mixing' (or 'only bio-irrigation') run and the 'always bioturbated' run. (e) δ^{56}Fe signature of the benthic DFe flux plotted against the benthic DFe flux. The dashed line shows a Rayleigh fractionation model ($\delta^{56}Fe - J_{DFe} = (1000.0 + 0.0)(1 - fr^{\alpha_{FeOOH-DFe}}) / (1 - fr) - 1000.0$, where fr is the remaining fraction of FeOOH and $\alpha_{FeOOH\text{-}DFe}$= 0.9987, the fractionation of DIR). (f) burial flux of pyrite (B_{FeS2}) plotted against the benthic DFe flux. (g) δ^{56}Fe signature of buried pyrite (δ^{56}Fe-B_{FeS2}) plotted against the benthic DFe flux.

3.3 A predictive function of the isotopic composition of benthic iron fluxes

Next, we derive predictive functions based on the most important drivers of the benthic DFe flux and its isotopic signature: bioturbation, $[O_2]_{BW}$, C_{ox} and $J_{FeOOH,T}$. We do this for a seafloor with bioturbation ('the modern seafloor') and a seafloor without bioturbation ('the unbioturbated seafloor').

3.3.1 The modern bioturbated seafloor

We build on the study of Dale et al. (2015) who derived a transfer function to quantify the J_{DFe} as a function of C_{ox}, $J_{FeOOH,T}$, and $[O_2]_{BW}$ (Eq. [1]). We repeated the same experiment (changing $[O_2]_{BW}$ from 1 to 200 µM and C_{ox} from 0.4 and 13.2 mmol m^{-2} d^{-1}; Table 2), to derive a similar predictive function for the δ^{56}Fe value of J_{DFe} (δ^{56}Fe-J_{DFe}). Model results indicate that δ^{56}Fe-J_{DFe} behaves similarly to J_{DFe} (Figure 5d,e) and the transfer function for δ^{56}Fe-J_{DFe} is best described as:

$$\delta^{56}Fe - J_{DFe} = \frac{1.65\left(Cox^2 / [O_2]_{BW}\right)}{2.09 + \left(Cox^2 / [O_2]_{BW}\right)} - 1.67 \qquad [9]$$

where C_{ox} is in mmol m^{-2} d^{-1}, $[O_2]_{BW}$ is in µM and $\delta^{56}Fe\text{-}J_{DFe}$ is in ‰. This function is independent of J_{FeOOH} and explains 95% of the variance in the modelled isotope values (Figure 5f). The maximum expressed fractionation, relative to the $\delta^{56}Fe$ of the FeOOH entering the sediment, is -1.67 ‰ for the tested ranges of C_{ox} and $[O_2]_{BW}$. For instance, if the FeOOH deposited on the seafloor has a $\delta^{56}Fe$ of -1.0 ‰, the maximum value of $\delta^{56}Fe$ of the dissolved iron flux will be -2.67 ‰.

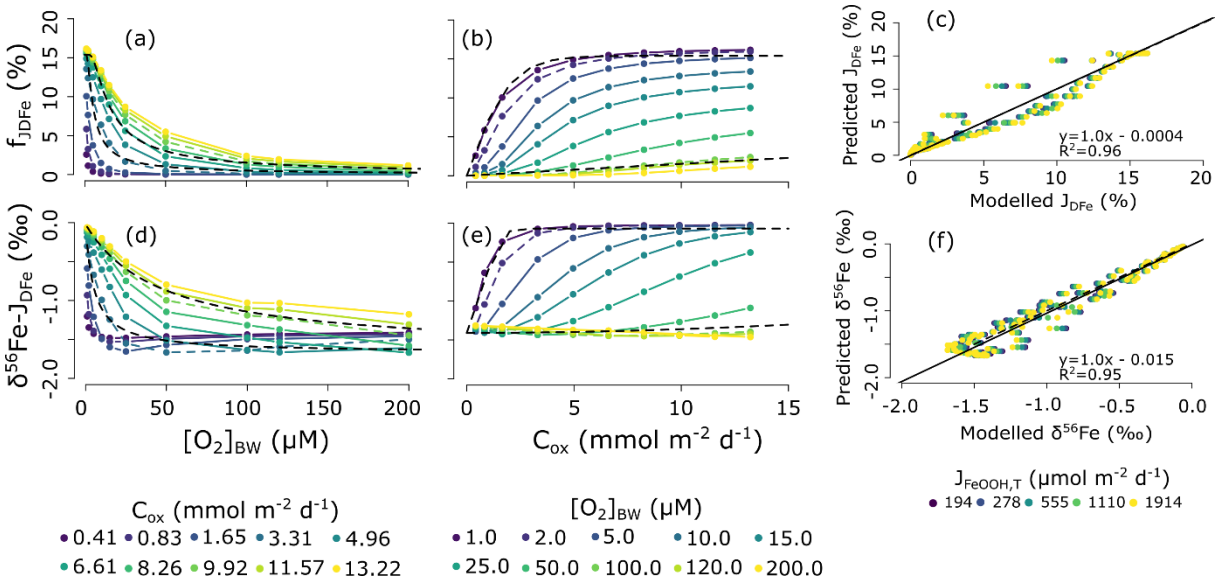

Figure 6: Simulated benthic DFe flux (J_{DFe}) (relative to the FeOOH influx; $J_{FeOOH,T}$) and the $\delta^{56}Fe$ signature of the DFe flux ($\delta^{56}Fe\text{-}J_{DFe}$) relative to (a),(d) bottom water oxygen concentrations ($[O_2]_{BW}$), (b),(e) carbon oxidation rate (C_{ox}) for a modern seafloor. In panels (a),(d) the results for C_{ox} = 3.31 mmol m^{-2} d^{-1} and C_{ox} = 9.92 mmol m^{-2} d^{-1} (dashed coloured lines) are compared to (Eq. [1] and [9] (dashed black lines). In panels (b),(e) the results for $[O_2]_{BW}$ = 2 µM and $[O_2]_{BW}$ = 100 µM (dashed coloured lines) are compared Eq. [1] and [9] (dashed black lines). Panels (c) and (f) show the correlation between the modelled (c) J_{DFe} and (f) $\delta^{56}Fe$, and the values predicted using the empirical functions (see main text).

3.3.2 An unbioturbated seafloor

Given that $J_{FeOOH,T}$ shows little impact on the model output of our previous experiments for the modern seafloor (Figure 5c,f), we do not repeat here the results of varying $J_{FeOOH,T}$ for an unbioturbated seafloor. Instead, we focus on the impact of $[SO_4^{2-}]_{BW}$ concentrations which varied from a few millimolar to 28 mM during the Phanerozoic (Wortmann & Paytan, 2012). Sulphate concentrations exert an important control on J_{DFe} because the major benthic sink for iron in sediments is its reaction with dissolved sulphides produced during the microbial reduction of

sulphate to iron-bound sulphides. The availability of sulphate in the sediment is thus expected to exert an important control on fraction of the DFe flux that can be trap in the sediment.

The global responses of J_{DFe} and $\delta^{56}Fe\text{-}J_{DFe}$ are broadly comparable to the modern bioturbated situation, although – as discussed in Section 3.2 – at higher $[O_2]_{BW}$, J_{DFe} is 30-40 % lower compared to bioturbated sediments (Figure 6a,b). We propose an asymptotic function to describe this behaviour,

$$J_{DFe} = \left(0.161 - 0.161e^{-3.67(C_{ox}/[O_2]_{BW})^{1.7}}\right) J_{FeOOH,T} \quad [10]$$

where C_{ox} is in mmol m^{-2} d^{-1}, $[O_2]_{BW}$ is in µM and J_{FeOOH} and J_{DFe} are in µmol m^{-2} d^{-1}. This function explains 98% of the variance in the modelled fluxes (Figure 6c). Surprisingly, decreasing $[SO_4^{2-}]_{BW}$ exerts a negligible impact on simulated J_{DFe} (Figure 6c). This suggests that, in unbioturbated sediments, re-oxidation of DFe in the oxic zone is more important than the trapping of DFe as iron-sulphide minerals. We observed a slight increase in J_{DFe} at higher $[SO_4^{2-}]_{BW}$ (points shift to the right in Figure 6c). This occurs because some oxidised iron minerals are not reactive towards organic matter, but can be reduced by dissolved sulphide (Berg et al., 2003; Canfield, 1989). By increasing sulphate concentrations, iron reduction is promoted via the sulphide intermediate, which leads to a slight increase in modelled J_{DFe}. In the absence of sulphide, some of the iron oxides could be reduced by oxidation of methane, although studies suggest that methane is not efficient at reducing iron compared to sulphide (Egger et al., 2014).

As expected, $\delta^{56}Fe\text{-}J_{DFe}$ trends relative to C_{ox} and $[O_2]_{BW}$ behave very similarly as J_{DFe} (Figure 6d,e), and consequently, the predictive function for the $\delta^{56}Fe\text{-}J_{DFe}$ resembles Eq. [10]

$$\delta^{56}Fe - J_{DFe} = \left(1.60 - 1.34e^{-3.67(C_{ox}/[O_2]_{BW})^{2.0}}\right) - 1.67 \quad [11]$$

where C_{ox} is in mmol m^{-2} d^{-1}, $[O_2]_{BW}$ is in µM and $\delta^{56}Fe\text{-}J_{DFe}$ is in ‰. This function explains 97% of the variance in the modelled fluxes (Figure 6f). Note that for $[O_2]_{BW}$ > 100 µM, $\delta^{56}Fe\text{-}J_{DFe}$ is

essentially invariant, which implies that $[O_2]_{BW}$ alone is a poor predictor for δ^{56}Fe-J_{DFe} at these O_2 levels.

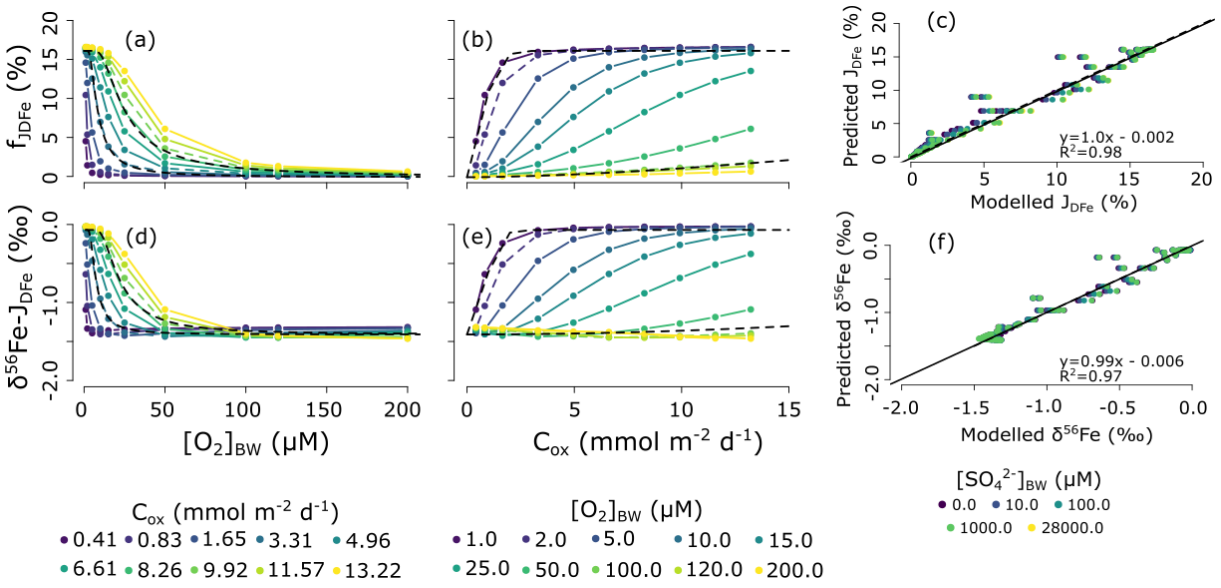

Figure 7: Simulated benthic DFe flux (J_{DFe}) (relative to the FeOOH influx; $J_{FeOOH,T}$) and the δ^{56}Fe signature of the DFe flux (δ^{56}Fe-J_{DFe}) relative to (a),(d) bottom water oxygen concentrations ($[O_2]_{BW}$), (b),(e) carbon oxidation rate (C_{ox}) for a Precambrian seafloor. The dashed black line in panels (a),(b),(d),(e) are the proposed functions for the magnitude (a),(b) and the δ^{56}Fe signature (d),(e) of the benthic DFe flux. In panels (a),(d) the results for C_{ox} = 3.31 mmol m^{-2} d^{-1} and C_{ox} = 9.92 mmol m^{-2} d^{-1} (dashed coloured lines) are compared to the new functions in Eq. [10] and [11]. In panels (b),(e) the results for $[O_2]_{BW}$ = 2 µM and $[O_2]_{BW}$ = 100 µM (dashed coloured lines) are compared to the new functions in Eq. [10] and [11]. Panels (c) and (f) show the correlation between the modelled (c) J_{DFe} and (f) δ^{56}Fe, and the values predicted from the empirical functions (see main text).

3.4 Importance of bioturbation for the global iron cycle

The predictive functions derived in Section 3.3 allow the influence of bioturbation on benthic DFe release and its δ^{56}Fe signature on the global scale to be assessed. We calculated the mean and total DFe flux (J_{DFe}) for several water depth intervals, as well as the mean δ^{56}Fe signature of the DFe flux (Table 4). Dissolved Fe fluxes for an unbioturbated seafloor (Global total: 70 Gmol Fe yr^{-1}) are much lower than for the modern seafloor (Global total: 158 Gmol Fe yr^{-1}) (Figure 7a,b). The mean unbioturbated J_{DFe} is around 1/3 of the mean bioturbated J_{DFe} in the deeper regions of the oceans (Table 4), where high oxygen concentrations and lower organic carbon oxidation rates prevent diffusional release of DFe. In the shallower shelf regions, DFe fluxes are in a similar range, but the mean J_{DFe} is still 1.8 times higher in bioturbated conditions (Table 4). Overall, global benthic DFe release for an unbioturbated seafloor is < 50 % of the global benthic DFe flux of the

587 modern seafloor (Table 4), which suggests that benthic fauna is an essential part of the modern
588 global marine iron cycle, and could be an important Fe source in Fe-limited regions.

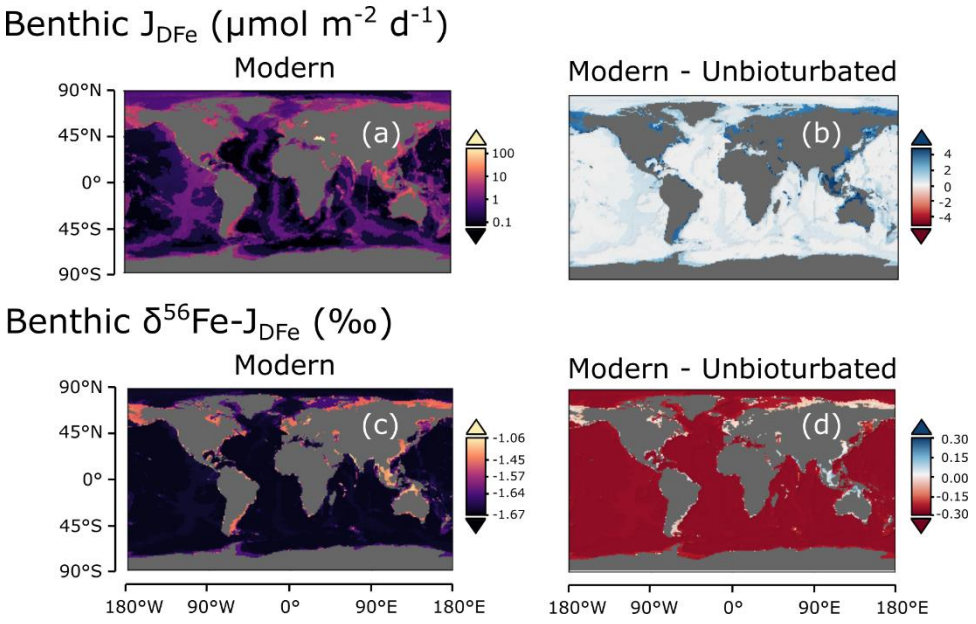

589

590 **Figure 8**: Top row: Benthic DFe fluxes (J_{DFe}). (a) The modern seafloor. (b) The difference between in J_{DFe} between
591 the modern scenario and an unbioturbated seafloor. Positive values mean J_{DFe} is higher in the modern scenario. Bottom
592 row: δ^{56}Fe signature of the benthic DFe flux (δ^{56}Fe-J_{DFe}). (c) The modern seafloor. (d) The difference in δ^{56}Fe-J_{DFe}
593 between the modern scenario and an unbioturbated seafloor. Positive values indicate a heavier isotopic signature for
594 the modern scenario. (a) is calculated with Eq. [1], (b) with Eq. [10], (c) with Eq. [9] and (d) is calculated Eq. [11].

595

596 Additionally, bioturbation increases the range in δ^{56}Fe values from DFe released from the
597 seafloor (Table 5). Indeed, our model experiments show that δ^{56}Fe-J_{DFe} values are near ~ -1.41 ‰
598 for $[O_2]_{BW}$ > 50 µM, and only show some variability below that oxygen concentration (Figure 5d).
599 In contrast, with bioturbation, δ^{56}Fe-J_{DFe} values show significant variability at all oxygen
600 concentrations (Figure 4d). Regardless of the range, both bioturbated as unbioturbated scenarios
601 show similar spatial trends. Lighter δ^{56}Fe values are found in the deep sea, where J_{DFe} is lower,
602 whereas heavier δ^{56}Fe values are found near shore, where J_{DFe} is higher (Figure 7c,d; Table 4).
603 Overall, the δ^{56}Fe signatures of J_{DFe} are consistently lighter (up to 0.3 ‰) in the modern seafloor
604 (Figure 7c,d; Table 4).

605 Overall, our results suggest that the evolution of benthic fauna and the advent of
606 bioturbation around the Ediacaran-Cambrian transition could have significantly altered the oceanic
607 iron cycle. Sediment mixing and burrow flushing by benthic fauna would have increased the

release of DFe from the seafloor, thereby stimulating Fe cycling in the water column and potentially increasing the residence time of Fe in the ocean. Our work adds to a growing body of literature that suggests that the burrowing revolution around the Ediacaran-Cambrian transition had a major impact on the global cycling of sulphur, carbon, phosphorus and oxygen (Boyle et al., 2014; Canfield & Farquhar, 2009; Dale et al., 2016; McIlroy & Logan, 1999; Meysman et al., 2006; van de Velde et al., 2018). Bioturbation has been suggested to increase phosphorus burial in marine sediments (although this is debated; Tarhan et al., 2021; van de Velde, James, et al., 2021), which could have limited primary productivity in the early Cambrian, consequently leading to lower atmospheric oxygen concentrations (Boyle et al., 2014; Dale et al., 2016; van de Velde et al., 2018). Our results suggest that the impact of bioturbation on the Fe cycle could have had the opposite effect. By increasing DFe release from the sediment, bioturbation could have relaxed iron limitation, potentially stimulating primary productivity in Fe-limited regions of the ocean.

Table 5: Dissolved iron fluxes and $d^{56}Fe$ signatures from marine sediments for a modern seafloor (calculated using Eq. [1] and [9]) and for an unbioturbated seafloor without bioturbation (calculated using Eq. [10] and [11]).

	Area [a] (10^{12} m^2)	Mean Cox [b] (mmol m^{-2} d^{-1})	Mean DFe Flux (µmol m^{-2} d^{-1})		Total DFe Flux [c] (Gmol yr^{-1})		Mean $\delta^{56}Fe\text{-}J_{DFe}$ (‰)	
			Modern	Unbioturbated	Modern	Unbioturbated	Modern	Unbioturbated
Shelf (0-200 m)	27.12	9.4	7.57	4.11	75 ± 38	41 ± 20	-1.42	-1.39
Upper slope (200 – 1000 m)	16.01	3.0	3.09	1.37	18 ± 9	8.0 ± 4.0	-1.63	-1.40
Lower slope (1000 – 2000 m)	15.84	1.5	2.03	0.64	12 ± 6	3.7 ± 1.8	-1.66	-1.41
Deep sea (> 2000 m)	302.5	0.4	0.48	0.16	53 ± 26	17 ± 8.5	-1.67	-1.41
Total					**158 ± 47**	**70 ± 22**		

[a] (Menard & Smith, 1966) [b] (Burdige, 2007) [c] Relative error on the benthic Fe flux, calculated using Eq. [1], was estimated at 50 % by Dale et al. (2015), based on the uncertainty in sedimentary Fe contents reported by Poulton & Raiswell (2002). Dale et al (2015) predicted a similar global flux of 150 ± 75 Gmol yr^{-1}.

3.5 Deoxygenation and the future global iron cycle

Since the 1950s, the global ocean oxygen inventory has decreased by a few percent, and low-oxygen zones have been expanding (Limburg et al., 2020). This ocean deoxygenation is driven by a decrease in O_2 solubility in warmer water and increasing eutrophication of coastal zones, which stimulates oxygen demand in the waters underlying the photic zone (Breitburg et al., 2018). Future climate change is expected to further exarcebate this problem; under a high emission

scenario – 8.5°C warming by the end of the century – Earth System models predict an globally averaged decrease of ~15 µM O_2 in the ocean.

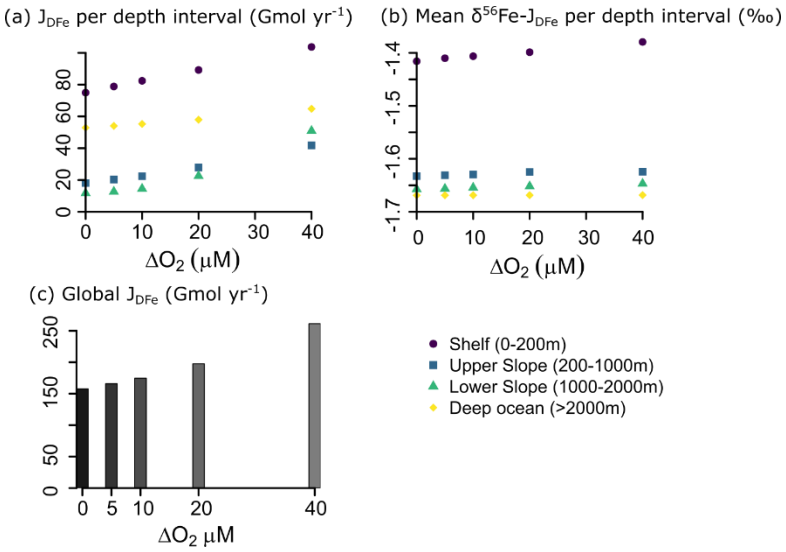

Figure 9: Effect of decreasing ocean oxygen concentrations on (a) the magnitude of DFe release from sediments per bathymetric depth interval, (b) the mean isotopic signature of the benthic DFe flux per bathymetric depth interval and (c) the global amount of DFe released from marine sediments.

Reducing $[O_2]_{BW}$ leads to higher DFe release from the seafloor (Figure 8a). Shelf and slope sediments (< 2000m) are more sensitivite to decreasing oxygen than deep-sea sediments (Figure 8a). Deep-sea sediments are generally well oxygenated (>200 µM O_2), and decreasing $[O_2]$ with 40 µM will have little effect on the release of DFe (Figure 5a). In contrast, slope sediments show more than a doubling of DFe release when O_2 is decreased by 40 µM, indicating their sensitivity to expanding low-oxygen zones. The mean δ^{56}Fe signature of J_{DFe} is however less affected by the decrease in oxygen and is likely more controlled by the sedimentary carbon oxidation rate that we applied per bathymetric depth interval (Table 5). The global amount of DFe released from the seafloor almost doubles, from 158 Gmol yr^{-1} today to 261 Gmol yr^{-1} for a 40 µM decrease in $[O_2]$. Note that decreasing $[O_2]$ equally for each gridcell is not realistic, as some regions – such as higher latitudes and the North Pacific – will experience stronger deoxygenation than equatorial regions (Kwiatkowski et al., 2020). Our simple exercise thus suggests that ongoing deoxygenation could have an important effect on the oceanic Fe cycle, potentially leading to an increase in ocean Fe inventory, and an increase in primary productivity.

4 Limitations

The model applied here was able to reproduce sedimentary profiles and isotope patterns of dissolved and particulate Fe species in two contrasting field sites. We derived fractionation factors that are fully consistent with laboratory experiments. Upscaling of our model results provides global flux estimates that are consistent with the current literature. Nevertheless, our approach is also subject to a number of limitations one should be aware of.

Firstly, the data availability for model calibration/validation is still limited. There are currently no datasets available that include isotope measurements for pore-water and solid-phase concentrations, as well as *in-situ* fluxes (collected at the same time and at athe same site). As a result, the model has only been calibrated on data from two shallow field sites (Table 3) and its applicability to deeper sediments (<1 km) thus remains untested.

Secondly, we do not explicitly test the influence of changes in OM reactivity on DFe fluxes and their isotopic signature. The model uses a a fixed reactivity distribution for organic matter. that is representative for fresh phytoplankton material that mostly degrades with a half-life of around two years (Boudreau & Ruddick, 1991; Dale et al., 2015). This parametrisation thus overestimates OM reactivity in depositional settings that receive large loads of less reactive terrestrial, physically protected and/or pre-aged OM. We also do not take into account any potential effects of bioturbation or anoxic conditions on the degradation of organic matter (Canfield, 1994; van de Velde, Hidalgo-Martinez, et al., 2020). Because the controls on organic matter reactivity in sediments are still a matter of extensive debate (see e.g. LaRowe et al., 2020), and outside the scope of this paper, we chose to keep organic matter reactivity fixed. We expect our choice of organic matter reactivity to have a limited impact on sediments < 1000 m because the vertical distribution of the diagenetic reations for a given sedimentary organic matter mineralisation rate would be largely determined by the most reactive fraction (and likely marine). It could however lead to an overestimation of the benthic Fe flux at waterdepths > 1000 m. Nevertheless, the estimated benthic flux for deep-sea sediments is $< 0.5 – 2.0$ µmol DFe m^{-2} d^{-1} (Table 4), which is in the range of DFe fluxes estimated from non-reductive dissolution of FeOOH (Homoky et al., 2013), a potentially important DFe source in these low-productive sediments. This would impact the δ^{56}Fe signature of the benthic DFe flux (which is ~0 ‰ for non-reductive dissolution), although the low flux magnitude means the impact on the oceanic δ^{56}Fe is expected to be small. In addition,

682 the derived transfer functions are based on depth-integrated degradation rates C_{ox} and thus
683 implicitly account for changes in OM flux and/or reactivity.

684 Finally, we assumed that the depositional flux of FeOOH is uniform over the whole
685 seafloor. However, in reality, deposition of FeOOH is not uniform, but varies geographically
686 (Hayes et al., 2021). This choice would, however, only affect the estimated global flux (Table 4),
687 and not our conclusions on the relative impact of bioturbation on sedimentary Fe release, nor the
688 isotope patterns (as these are independent of the FeOOH influx; Section 3.3.1). This issue could
689 be addressed by coupling the proposed benthic Fe flux equations to a pelagic Fe model (such as
690 cGEnIE.muffin; van de Velde, Hülse, et al., 2021), and would greatly improve global benthic Fe
691 flux predictions.

692 **5 Conclusions and outlook**

693 In this study, we assess the influence of bioturbation for benthic dissolved iron (DFe) fluxes
694 and their isotopic signature using reaction-transport modelling. Our derived fractionation factors
695 for iron reduction (-1.3‰), iron oxidation (+0.4‰), iron sulphide precipitation (+0.5‰) and
696 dissolution (-0.5‰) and pyrite precipitation (-0.7‰) were fully consistent with experimentally-
697 derived values. This suggests that the reported fractionations are robust, but the lack of available
698 field data indicates that more field studies measuring isotopes of pore-water Fe, solid-phase Fe and
699 benthic Fe fluxes from different depositional environments are needed.

700 We found that the influence of bioturbation on DFe fluxes depends on the redox state of
701 bottom waters. Bio-mixing reduces benthic DFe release and gives it a lighter isotopic signature at
702 low bottom water oxygen concentrations (<50 µM), whereas the combination of bio-mixing and
703 bio-irrigation increases benthic DFe release and gives it a heavier isotopic signature burial at higher
704 bottom water oxygen concentrations (>50 µM) (by stimulating FeS_2 burial). Globally, bioturbation
705 more than doubles the global benthic DFe flux (from 70 to 158 Gmol yr^{-1}) and decreases its
706 isotopic signature. Our results emphasise the global importance of bioturbating fauna as
707 ecosystems engineers and should inspire future research on the impact of environmental change
708 on the global iron cycle.

709 The predictive functions developed here can easily be applied to models of the modern and
710 past oceanic Fe cycle and help advance our understanding of the marine iron cycle. More

specifically, coupling our function to a pelagic iron model could predict spatial isotope patterns of dissolved and mineral Fe phases. This would be of major importance for the interpretation of Fe isotope patterns in the geological record, by explicitly accounting for close benthic-pelagic coupling where iron released from the seafloor is re-oxidised in the water column and rains back down on the sediment - such as during iron shelf-to-basin shuttling in low-oxygen oceans (Böning et al., 2020; Scholz, Severmann, et al., 2014).

Acknowledgments, Samples, and Data

The lead author would like to thank his family in New Zealand for providing him with a home (office) during the 2020 lockdown, which allowed him to conceive and develop this study.

The code for of the diagenetic model used in this paper is tagged as v0.1.0 and is assigned a DOI: https://doi.org/ 10.5281/zenodo.4953500 (van de Velde, 2021). The code is hosted on GitHub and can be obtained by cloning https://github.com/sevdevel/DiageneticIronIsotopeModel and then checking out the specific release 'git checkout v0.1.0'. All source code and simulation files required to reproduce the model results presented in this manuscript are stored in the main directory, details are given in the 'readme.txt' file in the main directory.

References

Aller, R. C. (2001). Transport and reactions in the bioirrigated zone. In B. P. Boudreau & B. B. Jorgensen (Eds.), *The Benthic Boundary Layer* (pp. 269–301). Oxford University Press.

Aller, R. C., & Aller, J. Y. (1998). The effect of biogenic irrigation intensity and solute exchange on diagenetic reaction rates in marine sediments. *Journal of Marine Research*, *56*(4), 905–936. https://doi.org/10.1357/002224098321667413

Balci, N., Bullen, T. D., Witte-Lien, K., Shanks, W. C., Motelica, M., & Mandernack, K. W. (2006). Iron isotope fractionation during microbially stimulated Fe(II) oxidation and Fe(III) precipitation. *Geochimica et Cosmochimica Acta*, *70*(3), 622–639. https://doi.org/10.1016/j.gca.2005.09.025

Beam, J. P., Scott, J. J., McAllister, S. M., Chan, C. S., McManus, J., Meysman, F. J. R., & Emerson, D. (2018). Biological rejuvenation of iron oxides in bioturbated marine sediments. *ISME Journal*, *12*(5), 1389–1394. https://doi.org/10.1038/s41396-017-0032-6

Beard, B. L., Johnson, C. M., Cox, L., Sun, H., Nealson, K. H., & Aguilar, C. (1999). Iron isotope biosignatures. *Science*, *285*(5435), 1889–1891. https://doi.org/10.1126/science.285.5435.1889

Beard, B. L., Johnson, C. M., Skulan, J. L., Nealson, K. H., Cox, L., & Sun, H. (2003). Application of Fe isotopes to tracing the geochemical and biological cycling of Fe. *Chemical Geology*, *195*(1–4), 87–117. https://doi.org/10.1016/S0009-2541(02)00390-X

Beard, B. L., Johnson, C. M., Von Damm, K. L., & Poulson, R. L. (2003). Iron isotope constraints on Fe cycling and mass balance in oxygenated Earth oceans. *Geology*, *31*(7),

629–632. https://doi.org/10.1130/0091-7613(2003)031<0629:IICOFC>2.0.CO;2

Berelson, W., McManus, J., Coale, K., Johnson, K., Burdige, D., Kilgore, T., et al. (2003). A time series of benthic flux measurements from Monterey Bay, CA. *Continental Shelf Research*, *23*(5), 457–481. https://doi.org/10.1016/S0278-4343(03)00009-8

Berg, P., Rysgaard, S., & Thamdrup, B. (2003). Dynamic Modeling of Early Diagenesis and Nutrient Cycling. A Case Study in an Artic Marine Sediment. *American Journal of Science*, *303*(10), 905–955. https://doi.org/10.2475/ajs.303.10.905

Berner, R. A., & Westrich, J. T. (1985). Bioturbation and the early diagenesis of carbon and sulfur. *American Journal of Science*, *285*, 193–206. https://doi.org/10.2475/ajs.285.3.193

Bohlen, L., Dale, A. W., Sommer, S., Mosch, T., Hensen, C., Noffke, A., et al. (2011). Benthic nitrogen cycling traversing the Peruvian oxygen minimum zone. *Geochimica et Cosmochimica Acta*, *75*(20), 6094–6111. https://doi.org/10.1016/j.gca.2011.08.010

Böning, P., Schnetger, B., Belz, L., Ferdelman, T., Brumsack, H. J., & Pahnke, K. (2020). Sedimentary iron cycling in the Benguela upwelling system off Namibia. *Earth and Planetary Science Letters*, *538*, 116212. https://doi.org/10.1016/j.epsl.2020.116212

Boudreau, B. P. (1984). On the equivalence of nonlocal and radial-diffusion models for porewater irrigation. *Journal of Marine Research*, *42*(3), 731–735. https://doi.org/10.1357/002224084788505924

Boudreau, B. P., & Ruddick, B. R. (1991). On a reactive continuum representation of organic matter diagenesis. *American Journal of Science*, *291*(5), 507–538. https://doi.org/10.2475/ajs.291.5.507

Boyd, P. W., Ellwood, M. J., Tagliabue, A., & Twining, B. S. (2017, March 1). Biotic and abiotic retention, recycling and remineralization of metals in the ocean. *Nature Geoscience*. Nature Publishing Group. https://doi.org/10.1038/ngeo2876

Boyle, R. A., Dahl, T. W., Dale, A. W., Zhu, M., Brasier, M. D., Canfield, D. E., & Lenton, T. M. (2014). Stabilization of the coupled oxygen and phosphorus cycles by the evolution of bioturbation. *Nature Geoscience*, *7*(August), 671–676. https://doi.org/10.1038/NGEO2213

Breitburg, D., Levin, L. A., Oschlies, A., Grégoire, M., Chavez, F. P., Conley, D. J., et al. (2018, January 5). Declining oxygen in the global ocean and coastal waters. *Science*. American Association for the Advancement of Science. https://doi.org/10.1126/science.aam7240

Bullen, T. D., White, A. F., Childs, C. W., Vivit, D. V., & Schultz, M. S. (2001). Demonstration of significant abiotic iron isotope fractionation in nature. *Geology*, *29*(8), 699–702. https://doi.org/10.1130/0091-7613(2001)029<0699:DOSAII>2.0.CO;2

Burdige, D. J. (2007). Preservation of Organic Matter in Marine Sediments: Controls, Mechanisms, and an Imbalance in Sediment Organic Carbon Budgets? *Chemical Reviews*, *107*(January), 467–485. https://doi.org/10.1021/cr050347q

Burdige, D. J., & Komada, T. (2020). Iron redox cycling, sediment resuspension and the role of sediments in low oxygen environments as sources of iron to the water column. *Marine Chemistry*, *223*, 103793. https://doi.org/10.1016/j.marchem.2020.103793

Burwicz, E. B., Rüpke, L. H., & Wallmann, K. (2011). Estimation of the global amount of

submarine gas hydrates formed via microbial methane formation based on numerical reaction-transport modeling and a novel parameterization of Holocene sedimentation. *Geochimica et Cosmochimica Acta*, *75*(16), 4562–4576. https://doi.org/10.1016/j.gca.2011.05.029

Butler, I. B., Archer, C., Vance, D., Oldroyd, A., & Rickard, D. (2005). Fe isotope fractionation on FeS formation in ambient aqueous solution. *Earth and Planetary Science Letters*, *236*(1–2), 430–442. https://doi.org/10.1016/j.epsl.2005.05.022

Canfield, D. E. (1989). Reactive iron in marine sediments. *Geochimica et Cosmochimica Acta*, *53*, 619–632. https://doi.org/10.1016/0016-7037(89)90005-7

Canfield, D. E. (1994). Factors influencing organic carbon preservation in marine sediments. *Chemical Geology*, *114*, 315–329.

Canfield, D. E., & Farquhar, J. (2009). Animal evolution, bioturbation, and the sulfate concentration of the oceans. *Proceedings of the National Academy of Sciences*, *106*(20), 8123–8127.

Canfield, D. E., Raiswell, R., & Bottrell, S. H. (1992). The reactivity of sedimentary iron minerals toward sulfide. *American Journal of Science*, *292*, 659–683.

Canfield, D. E., Thamdrup, B., & Hansen, J. W. (1993). The anaerobic degradation of organic matter in Danish coastal sediments: iron reduction, manganese reduction, and sulfate reduction. *Geochimica et Cosmochimica Acta*, *57*(16), 3867–3883. https://doi.org/10.1016/0016-7037(93)90340-3

Van Cappellen, P., & Wang, Y. (1995). Metal cycling in surface sediments: Modeling the interplay of transport and reaction. In H. E. Allen (Ed.), *Metal Contaminated Aquatic Sediments* (pp. 21–64). Ann Arbor Press.

Conway, T. M., & John, S. G. (2014). Quantification of dissolved iron sources to the North Atlantic Ocean. *Nature*, *511*(7508), 212–215. https://doi.org/10.1038/nature13482

Crosby, H. A., Johnson, C. M., Roden, E. E., & Beard, B. L. (2005). Coupled Fe(II)-Fe(III) electron and atom exchange as a mechanism for Fe isotope fractionation during dissimilatory iron oxide reduction. *Environmental Science and Technology*, *39*(17), 6698–6704. https://doi.org/10.1021/es0505346

Crosby, H. A., Roden, E. E., Johnson, C. M., & Beard, B. L. (2007). The mechanisms of iron isotope fractionation produced during dissimilatory Fe(III) reduction by Shewanella putrefaciens and Geobacter sulfurreducens. *Geobiology*, *5*(2), 169–189. https://doi.org/10.1111/j.1472-4669.2007.00103.x

Dale, A. W., Nickelsen, L., Scholz, F., Hensen, C., Oschlies, A., & Wallmann, K. (2015). A revised global estimate of dissolved iron fluxes from marine sediments. *Global Biogeochemical Cycles*, *29*, 1–17. https://doi.org/10.1002/2013GB004679.Received

Dale, A. W., Boyle, R. A., Lenton, T. M., Ingall, E. D., & Wallmann, K. (2016). A model for microbial phosphorus cycling in bioturbated marine sediments : Significance for phosphorus burial in the early Paleozoic. *Geochimica et Cosmochimica Acta*, *189*, 251–268. https://doi.org/10.1016/j.gca.2016.05.046

Dauphas, N., John, S. G., & Rouxel, O. (2017). Iron isotope systematics. *Reviews in Mineralogy*

& Geochemistry, *82*, 415–510. https://doi.org/10.2138/rmg.2017.82.11

Egger, M., Rasigraf, O., Sapart, C. J., Jilbert, T., Jetten, M. S. M., Röckmann, T., et al. (2014). Iron-Mediated Anaerobic Oxidation of Methane in Brackish Coastal Sediments. *Environmental Science & Technology*, *2014*(1).

Elrod, V. A., Berelson, W. M., Coale, K. H., & Johnson, K. S. (2004). The flux of iron from continental shelf sediments: A missing source for global budgets. *Geophysical Research Letters*, *31*(12), 2–5. https://doi.org/10.1029/2004GL020216

Gartman, A., & Findlay, A. J. (2020). Impacts of hydrothermal plume processes on oceanic metal cycles and transport. *Nature Geoscience*. https://doi.org/10.1038/s41561-020-0579-0

Guilbaud, R., Butler, I. B., & Ellam, R. M. (2011). Abiotic pyrite formation produces a large Fe isotope fractionation. *Science*, *332*(6068), 1548–1552. https://doi.org/10.1126/science.1202924

Hayes, C. T., Costa, K. M., Anderson, R. F., Calvo, E., Chase, Z., Demina, L. L., et al. (2021). Global Ocean Sediment Composition and Burial Flux in the Deep Sea. *Global Biogeochemical Cycles*, *35*, e2020GB006769. https://doi.org/10.1029/2020gb006769

Homoky, W. B., John, S. G., Conway, T. M., & Mills, R. A. (2013). Distinct iron isotopic signatures and supply from marine sediment dissolution. *Nature Communications*, *4*. https://doi.org/10.1038/ncomms3143

Homoky, W. B., Weber, T., Berelson, W. M., Conway, T. M., Henderson, G. M., Van Hulten, M., et al. (2016). Quantifying trace element and isotope fluxes at the ocean-sediment boundary: a review. *Philosophical Transactions of the Royal Society of London A: Mathematical, Physical and Engineering Sciences*, *374*(20160246). https://doi.org/10.1098/rsta.2016.0246

Icopini, G. A., Anbar, A. D., Ruebush, S. S., Tien, M., & Brantley, S. L. (2004). Iron isotope fractionation during microbial reduction of iron: The importance of adsorption. *Geology*, *32*(3), 205–208. https://doi.org/10.1130/G20184.1

John, S. G., Mendez, J., Moffett, J., & Adkins, J. (2012). The flux of iron and iron isotopes from San Pedro Basin sediments. *Geochimica et Cosmochimica Acta*, *93*, 14–29. https://doi.org/10.1016/j.gca.2012.06.003

Johnson, C. M., Roden, E. E., Welch, S. A., & Beard, B. L. (2004). Experimental constraints on Fe isotope fractionation during magnetite and Fe carbonate formation coupled to dissimilatory hydrous ferric oxide reduction. *Geochimica et Cosmochimica Acta*, *69*(4), 963–993. https://doi.org/10.1016/j.gca.2004.06.043

Jorgensen, B. B. (1979). A theoretical model of the stable sulfur isotope distribution in marine sediments. *Geochimica et Cosmochimica Acta*, *43*(3), 363–374. https://doi.org/10.1016/0016-7037(79)90201-1

Kristensen, E., Penha-Lopes, G., Delefosse, M., Valdemarsen, T., Quintana, C. O., & Banta, G. T. (2012). What is bioturbation? the need for a precise definition for fauna in aquatic sciences. *Marine Ecology Progress Series*, *446*, 285–302. https://doi.org/10.3354/meps09506

Kwiatkowski, L., Torres, O., Bopp, L., Aumont, O., Chamberlain, M., R. Christian, J., et al.

(2020). Twenty-first century ocean warming, acidification, deoxygenation, and upper-ocean nutrient and primary production decline from CMIP6 model projections. *Biogeosciences, 17*(13), 3439–3470. https://doi.org/10.5194/bg-17-3439-2020

LaRowe, D. E., Arndt, S., Bradley, J. A., Estes, E. R., Hoarfrost, A., Lang, S. Q., et al. (2020, May 1). The fate of organic carbon in marine sediments - New insights from recent data and analysis. *Earth-Science Reviews*. Elsevier B.V. https://doi.org/10.1016/j.earscirev.2020.103146

Lenstra, W. K., Hermans, M., Seguret, M., Witbaard, R., Behrends, T., Helmond, N. A. G. M. Van, et al. (2018). The shelf-to-basin iron shuttle in the Black Sea revisited. *Chemical Geology*, 1–52. https://doi.org/10.1016/j.chemgeo.2018.10.024

Limburg, K. E., Breitburg, D., Swaney, D. P., & Jacinto, G. (2020). Ocean Deoxygenation: A Primer. *One Earth, 2*(1), 24–29. https://doi.org/10.1016/j.oneear.2020.01.001

Mahowald, N. M., Baker, A. R., Bergametti, G., Brooks, N., Duce, R. A., Jickells, T. D., et al. (2005, December 1). Atmospheric global dust cycle and iron inputs to the ocean. *Global Biogeochemical Cycles*. John Wiley & Sons, Ltd. https://doi.org/10.1029/2004GB002402

Mansor, M., & Fantle, M. S. (2019). A novel framework for interpreting pyrite-based Fe isotope records of the past. *Geochimica et Cosmochimica Acta, 253*, 39–62. https://doi.org/10.1016/j.gca.2019.03.017

Martin, J. H. (1990). *Glacial-Interglacial CO2 change: the iron hypothesis*. *Paleoceanography* (Vol. 5).

McIlroy, D., & Logan, G. a. (1999). The impact of bioturbation on infaunal ecology and evolution during the Proterozoic-Cambrian transition. *Palaios, 14*(1), 58–72. https://doi.org/10.2307/3515361

Meile, C., Berg, P., Van Cappellen, P., & Tuncay, K. (2005). Solute-specific pore water irrigation: Implications for chemical cycling in early diagenesis. *Journal of Marine Research, 63*, 601–621. https://doi.org/10.1357/0022240054307885

Menard, H. W., & Smith, S. M. (1966). Hypsometry of Ocean Basin Provinces. *Journal of Geophysical Research, 71*(18), 4305–4325.

Meysman, F. J. R., Middelburg, J. J., Herman, P. M. J., & Heip, C. H. R. (2003). Reactive transport in surface sediments. II. Media: an object-oriented problem-solving environment for early diagenesis. *Computers & Geosciences, 29*(3), 301–318. https://doi.org/10.1016/S0098-3004(03)00007-4

Meysman, F. J. R., Boudreau, B. P., & Middelburg, J. J. (2005). Modeling reactive transport in sediments subject to bioturbation and compaction. *Geochimica et Cosmochimica Acta, 69*(14), 3601–3617. https://doi.org/10.1016/j.gca.2005.01.004

Meysman, F. J. R., Middelburg, J. J., & Heip, C. H. R. (2006). Bioturbation: a fresh look at Darwin's last idea. *Trends in Ecology & Evolution, 21*(12), 688–95. https://doi.org/10.1016/j.tree.2006.08.002

Meysman, F. J. R., Boudreau, B. P., & Middelburg, J. J. (2010). When and why does bioturbation lead to diffusive mixing ? *Journal of Marine Research, 68*, 881–920.

Pakhomova, S. V., Hall, P. O. J., Kononets, M. Y., Rozanov, A. G., Tengberg, A., & Vershinin, A. V. (2007). Fluxes of iron and manganese across the sediment-water interface under various redox conditions. *Marine Chemistry*, *107*(3), 319–331. https://doi.org/10.1016/j.marchem.2007.06.001

Poulton, S. W. (2003). Sulfide oxidation and iron dissolution kinetics during the reaction of dissolved sulfide with ferrihydrite. *Chemical Geology*, *202*(1–2), 79–94. https://doi.org/10.1016/S0009-2541(03)00237-7

Poulton, S. W., & Canfield, D. E. (2005). Development of a sequential extraction procedure for iron: Implications for iron partitioning in continentally derived particulates. *Chemical Geology*, *214*, 209–221. https://doi.org/10.1016/j.chemgeo.2004.09.003

Poulton, S. W., & Raiswell, R. (2002). The low-temperature geochemical cycle of iron: From continental fluxes to marine sediment deposition. *American Journal of Science*, *302*(9), 774–805. https://doi.org/10.2475/ajs.302.9.774

Poulton, S. W., Krom, M. D., & Raiswell, R. (2004). A revised scheme for the reactivity of iron (oxyhydr)oxide minerals towards dissolved sulfide. *Geochimica et Cosmochimica Acta*, *68*(18), 3703–3715. https://doi.org/10.1016/j.gca.2004.03.012

R Core Team. (2017). R: A Language and Environment for Statistical Computing.

Raiswell, R., & Canfield, D. E. (1998). Sources of iron for pyrite formation in marine sediments. *American Journal of Science*, *298*(3), 219–245. https://doi.org/10.2475/ajs.298.3.219

Raiswell, R., & Canfield, D. E. (2012). The Iron Biogeochemical Cycle Past and Present. *Geochemical Perspectives*, *1*(1), 1–232.

Reimers, C. E., Ruttenberg, K. C., Canfield, D. E., Christiansen, M. B., & Martin, J. B. (1996). Porewater pH and authigenic phases formed in the uppermost sediments of the Santa Barbara Basin. *Geochimica et Cosmochimica Acta*, *60*(21), 4037–4057. https://doi.org/10.1016/S0016-7037(96)00231-1

Rolison, J. M., Stirling, C. H., Middag, R., Gault-Ringold, M., George, E., & Rijkenberg, M. J. A. (2018). Iron isotope fractionation during pyrite formation in a sulfidic Precambrian ocean analogue. *Earth and Planetary Science Letters*, *488*, 1–13. https://doi.org/10.1016/j.epsl.2018.02.006

Scholz, F., Severmann, S., McManus, J., Noffke, A., Lomnitz, U., & Hensen, C. (2014). On the isotope composition of reactive iron in marine sediments: Redox shuttle versus early diagenesis. *Chemical Geology*, *389*(June 2019), 48–59. https://doi.org/10.1016/j.chemgeo.2014.09.009

Scholz, F., McManus, J., Mix, A. C., Hensen, C., & Schneider, R. R. (2014). The impact of ocean deoxygenation on iron release from continental margin sediments. *Nature Geoscience*, *7*(6), 433–437. https://doi.org/10.1038/ngeo2162

Schroth, A. W., Crusius, J., Sholkovitz, E. R., & Bostick, B. C. (2009). Iron solubility driven by speciation in dust sources to the ocean. *Nature Geoscience*, *2*(5), 337–340. https://doi.org/10.1038/ngeo501

Severmann, S., Johnson, C. M., Beard, B. L., & McManus, J. (2006). The effect of early diagenesis on the Fe isotope compositions of porewaters and authigenic minerals in

continental margin sediments. *Geochimica et Cosmochimica Acta*, *70*(8), 2006–2022. https://doi.org/10.1016/j.gca.2006.01.007

Severmann, S., McManus, J., Berelson, W. M., & Hammond, D. E. (2010). The continental shelf benthic iron flux and its isotope composition. *Geochimica et Cosmochimica Acta*, *74*(14), 3984–4004. https://doi.org/10.1016/j.gca.2010.04.022

Soetaert, K., & Meysman, F. (2012). Reactive transport in aquatic ecosystems: Rapid model prototyping in the open source software R. *Environmental Modelling and Software*, *32*, 49–60. https://doi.org/10.1016/j.envsoft.2011.08.011

Solan, M., Ward, E. R., White, E. L., Hibberd, E. E., Cassidy, C., Schuster, J. M., et al. (2019). Worldwide measurements of bioturbation intensity, ventilation rate, and the mixing depth of marine sediments. *Scientific Data*, *6*(1), 58. https://doi.org/10.1038/s41597-019-0069-7

Stevenson, E. I., Fantle, M. S., Das, S. B., Williams, H. M., & Aciego, S. M. (2017). The iron isotopic composition of subglacial streams draining the Greenland ice sheet. *Geochimica et Cosmochimica Acta*, *213*, 237–254. https://doi.org/10.1016/j.gca.2017.06.002

Tagliabue, A., Bopp, L., Dutay, J. C., Bowie, A. R., Chever, F., Jean-Baptiste, P., et al. (2010). Hydrothermal contribution to the oceanic dissolved iron inventory. *Nature Geoscience*, *3*(4), 252–256. https://doi.org/10.1038/ngeo818

Tagliabue, A., Aumont, O., DeAth, R., Dunne, J. P., Dutkiewicz, S., Galbraith, E., et al. (2016). How well do global ocean biogeochemistry models simulate dissolved iron distributions? *Global Biogeochemical Cycles*, *30*, 149–174. https://doi.org/10.1002/2015GB005289

Tagliabue, A., Bowie, A. R., Boyd, P. W., Buck, K. N., Johnson, K. S., & Saito, M. A. (2017, March 1). The integral role of iron in ocean biogeochemistry. *Nature*. Nature Publishing Group. https://doi.org/10.1038/nature21058

Tarhan, L. G., Zhao, M., & Planavsky, N. J. (2021). Bioturbation feedbacks on the phosphorus cycle. *Earth and Planetary Science Letters*, *566*, 116961. https://doi.org/10.1016/j.epsl.2021.116961

Thamdrup, B., Fossing, H., & Jorgensen, B. B. (1994). Manganese, iron, and sulfur cycling in a coastal marine sediment, Aarhus Bay, Denmark. *Geochimica et Cosmochimica Acta*, *58*(23), 5115–5129.

Thibault de Chanvalon, A., Metzger, E., Mouret, A., Knoery, J., Geslin, E., & Meysman, F. J. R. (2017). Two dimensional mapping of iron release in marine sediments at submillimetre scale. *Marine Chemistry*, *191*, 34–49. https://doi.org/10.1016/j.marchem.2016.04.003

Thullner, M., Dale, A. W., & Regnier, P. (2009). Global-scale quantification of mineralization pathways in marine sediments: A reaction-transport modeling approach. *Geochemistry, Geophysics, Geosystems*, *10*(10). https://doi.org/10.1029/2009GC002484

van de Velde, S. J. (2021). DiageneticIronIsotopeModel v0.1.0. Zenodo. https://doi.org/10.5281/zenodo.4953500

van de Velde, S. J., & Meysman, F. J. R. (2016). The influence of bioturbation on iron and sulphur cycling in marine sediments: a model analysis. *Aquatic Geochemistry*, *22*(5–6), 469–504. https://doi.org/10.1007/s10498-016-9301-7

van de Velde, S. J., Mills, B., Meysman, F. J., Lenton, T. M., & Poulton, S. W. (2018). Early Palaeozoic ocean anoxia and global warming driven by the evolution of shallow burrowing. *Nature Communications*, *9*, 2554. https://doi.org/10.1038/s41467-018-04973-4

van de Velde, S. J., Hidalgo-Martinez, S., Callebaut, I., Antler, G., James, R., Leermakers, M., & Meysman, F. (2020). Burrowing fauna mediate alternative stable states in the redox cycling of salt marsh sediments. *Geochimica et Cosmochimica Acta*, *276*, 31–49. https://doi.org/10.1016/j.gca.2020.02.021

van de Velde, S. J., Hylén, A., Kononets, M., Marzocchi, U., Leermakers, M., Choumiline, K., et al. (2020). Elevated sedimentary removal of Fe, Mn, and trace elements following a transient oxygenation event in the Eastern Gotland Basin, central Baltic Sea. *Geochimica et Cosmochimica Acta*, *271*, 16–32. https://doi.org/10.1016/j.gca.2019.11.034

van de Velde, S. J., James, R., Callebaut, I., Hidalgo-Martinez, S., & Meysman, F. (2021). Bioturbation has a limited effect on phosphorus burial in salt marsh sediments. *Biogeosciences*, *18*, 1451–1461. https://doi.org/10.5194/bg-18-1451-2021

van de Velde, S. J., Hülse, D., Reinhard, C. T., & Ridgwell, A. (2021). Iron and sulfur cycling in the cGENIE.muffin Earth system model (v0.9.21). *Geoscientific Model Development*, *14*, 2713–2745. https://doi.org/10.5194/gmd-14-2713-2021

Watson, A. J., Bakker, D. C. E., Ridgwell, A., Boyd, P. W., & Law, C. S. (2000). Effect of iron supply on Southern Ocean CO2 uptake and implications for glacial atmospheric CO2. *Nature*, *407*, 730–733. Retrieved from www.g-cubed.org

Welch, S. A., Beard, B. L., Johnson, C. M., & Braterman, P. S. (2003). Kinetic and equilibrium Fe isotope fractionation between aqueous Fe(II) and Fe(III). *Geochimica et Cosmochimica Acta*, *67*(22), 4231–4250. https://doi.org/10.1016/S0016-7037(03)00266-7

Wortmann, U. G., & Paytan, A. (2012). Rapid Variability of Seawater Chemistry Over the Past 130 Million Years Downloaded from. *Science*, *337*, 334–336. https://doi.org/10.1126/science.1220224

Wu, L., Druschel, G., Findlay, A., Beard, B. L., & Johnson, C. M. (2012). Experimental determination of iron isotope fractionations among Fe aq2+-FeS aq-Mackinawite at low temperatures: Implications for the rock record. *Geochimica et Cosmochimica Acta*, *89*, 46–61. https://doi.org/10.1016/j.gca.2012.04.047